

COSMOGLOBE DR2. III. Improved modelling of zodiacal light with COBE-DIRBE through global Bayesian analysis

M. San^{1*}, M. Galloway¹, E. Gjerløw¹, D. J. Watts¹, R. Aurlien¹, A. Basyrov¹, M. Brilenkov¹, H. K. Eriksen¹, U. Fuskeland¹, L. T. Hergt², D. Herman¹, H. T. Ihle¹, J. G. S. Lunde¹, S. K. Næss¹, N.-O. Stutzer¹, H. Thommesen¹, and I. K. Wehus¹

¹ Institute of Theoretical Astrophysics, University of Oslo, Blindern, Oslo, Norway

² Department of Physics and Astronomy, University of British Columbia, 6224 Agricultural Road, Vancouver BC, V6T1Z1, Canada

August 21, 2024

ABSTRACT

We present an improved zodiacal light (ZL) model for COBE-DIRBE derived through global Bayesian analysis within the COSMOGLOBE Data Release 2 (DR2) framework. The parametric form of the ZL model is identical to that introduced by Kelsall et al. (1998; K98), but the specific best-fit parameter values are re-derived using the combination of DIRBE Calibrated Individual Observations (CIO), *Planck* HFI sky maps, and WISE and *Gaia* compact object catalogs. Furthermore, the ZL parameters are fitted jointly with astrophysical parameters, such as thermal dust and starlight emission, and the new model takes into account excess radiation that appears stationary in solar-centric coordinates as reported in a companion paper. The relative differences between the predicted signals from K98 and our new model are $\lesssim 5\%$ in the 12 and 25 μm channels over the full sky. The zero-levels of the cleaned DR2 maps are lower than those of the K98 Zodiacal light Subtracted Mission Average (ZSMA) maps by $\sim 10 \text{ kJy/sr}$ at 1.25–3.5 μm , which is larger than the entire predicted contribution from high-redshift galaxies to the Cosmic Infrared Background (CIB) at the same wavelengths. The total RMS of each DR2 map at wavelengths up to and including 25 μm are $\sim 30\%$ lower at high Galactic latitudes than the corresponding DIRBE ZSMA maps. The cleaned DR2 maps at 4.9 and 12 μm are now, for the first time, visually dominated by Galactic signal at high latitudes rather than by ZL residuals. Even the 100 μm channel, which has served as a cornerstone for Galactic studies for three decades, appears significantly cleaner in the current processing. Still, obvious ZL residuals can be seen in several of the DR2 maps, and further work is required to mitigate these. Joint analysis with existing and future high-resolution full-sky surveys such as AKARI, IRAS, *Planck* HFI, and SPHEREx will be essential both to break key degeneracies in the current model and to determine whether the reported solar-centric excess radiation has a ZL or instrumental origin. On the algorithmic side, more efficient methods for probing massively multi-peaked likelihoods should be explored and implemented. Thus, while the results presented in this paper do redefine the state-of-the-art for DIRBE modelling, it also only represents the first among many steps toward a future optimal Bayesian ZL model.

Key words. Zodiacal dust, Interplanetary medium, Cosmology: cosmic background radiation

Contents

| | | | | | |
|----------|--|----------|---|---|-----------|
| 1 | Introduction | 1 | 5 | Results | 11 |
| 2 | Zodiacal light modelling | 2 | 5.1 | Markov chains | 11 |
| 2.1 | Parameterization of interplanetary dust | 2 | 5.2 | Updated ZL model | 14 |
| 2.2 | Zodiacal components | 3 | 5.3 | Goodness-of-fit | 16 |
| 2.3 | Radiative and scattering properties | 3 | 5.4 | Comparison of ZSMA maps | 18 |
| 2.4 | Model intuition | 4 | 6 | Conclusions | 20 |
| 2.5 | Numerical optimizations | 5 | A | Component-wise zodiacal light maps and number density cross-sections | 23 |
| 3 | Methods | 5 | B | Interplanetary dust parameter atlas | 26 |
| 3.1 | Data model, posterior distribution, and Gibbs sampling | 5 | 1. Introduction | | |
| 3.2 | Comparison with K98 fitting algorithm | 6 | Zodiacal light (ZL, sometimes zodiacal emission or interplanetary dust emission) is the primary source of diffuse radiation observed in the infrared sky between 1–100 μm (see, e.g., Leinert et al. 1998a and references therein). This radiation comes from scattering and re-emission of sunlight from interplanetary dust (IPD) grains, and was first mapped in detail by the IRAS satellite (Neugebauer et al. 1984). | | |
| 3.3 | Posterior sampling by non-linear optimization | 8 | The inner Solar system is embedded in a Sun centered cloud of IPD, with a symmetry axis tilted slightly with respect to the | | |
| 4 | Data | 9 | | | |
| 4.1 | DIRBE Calibrated Individual Observations | 9 | | | |
| 4.2 | Ancillary data | 10 | | | |
| 4.3 | Masks | 11 | | | |

* Corresponding author: M. San; metin.san@astro.uio.no

Ecliptic, known as the zodiacal cloud. The ZL is seasonal, and its appearance in the sky changes as the Earth moves through the IPD distribution. The most common way to model the observer position-dependent ZL is to evaluate a line-of-sight integral for each observation directly in the time-ordered domain. The time-varying and three-dimensional nature of the ZL makes it one of the most challenging foregrounds to model in astrophysical and cosmological studies of the infrared sky. The lack of a high-accuracy ZL model has left a large part of the electromagnetic spectrum inaccessible to cosmological analysis attempting to measure the Cosmic Infrared Background (CIB; Partridge & Peebles 1967; Hauser et al. 1998; Hauser & Dwek 2001).

One of the most widely used ZL models in the field of cosmology is the *COBE*-DIRBE model by Kelsall et al. (1998), often simply referred to as the K98 model. This is a parametric model that describes the three-dimensional distribution and radiative properties of IPD using time-dependent measurements from the *COBE*-DIRBE instrument (Hauser et al. 1998). There have been extensions to this model proposed since this original work, primarily to explain residual monopoles seen in comparisons to other data (Sano et al. 2020; Korngut et al. 2022; Carleton et al. 2022). Additionally, there have been several direct measurements of the IPD density (Poppe et al. 2019; Szalay et al. 2020), some of which suggest that the IPD densities may be greater than previously predicted (Nieto et al. 2005). Despite these potential shortcomings, the Kelsall model remains the default model in the CMB field today.

Since the DIRBE experiment, our understanding of the infrared sky has improved with new observational data from experiments like WISE (Wright et al. 2010), *Planck* HFI (Planck Collaboration III 2020), and *Gaia* (Gaia Collaboration et al. 2016). However, these experiments have largely been analyzed individually, and little or no coordinated effort has been made toward combining the data from these experiments into one overall state-of-the-art model of the infrared sky. The main goal of the current work, summarized in a series of papers collectively denoted COSMOGLOBE Data Release 2, is to make the first step toward such a concordance model by leveraging recent computational advances in Bayesian cosmological data analysis by the BEYONDPLANCK (BeyondPlanck Collaboration et al. 2023; Galloway et al. 2023, and references therein) and COSMOGLOBE (Watts et al. 2023) collaborations. The computer code implementation is called `Commander3` (Galloway et al. 2023), which is a Bayesian Gibbs sampler that was originally designed for end-to-end analysis of cosmic microwave background (CMB) experiments, in particular *Planck* LFI (Planck Collaboration II 2020) and *WMAP* (Bennett et al. 2013). However, as demonstrated in the current work, the same algorithms are, after relatively minor modifications, directly applicable to infrared measurements.

One of the most important generalizations required for application of `Commander3` to the infrared sky is the implementation of an accurate ZL model to remove the time-varying ZL. In this paper we therefore implement support for the K98 model in `Commander3`, and we apply this to the time-domain DIRBE data. This new code implementation is based on `ZodiPy` (San 2024), which is an Astropy-affiliated Python package for ZL simulations. As an early application of this framework, San et al. (2022) demonstrated the removal of ZL from the DIRBE time-ordered data (TOD) with `ZodiPy` using the K98 model.

ZL is found to be polarized in the near-infrared in both the DIRBE and *CIBER* data (Takimoto et al. 2022, 2023). We make no attempts at modeling polarized ZL in this analysis, but a natural next step in this analysis would be to include the polarization data from the 1.25, 2.2, and 3.9 μm DIRBE bands.

The rest of the paper is organized as follows. In Sect. 2, we introduce the K98 ZL model and discuss implementation and optimization aspects. Next, in Sect. 3, we describe the algorithms and methods used to fit the ZL parameters within the COSMOGLOBE framework. In Sect. 4, we describe the data used in the current analysis. Next, in Sect. 5, we present our updated ZL model and compare this with the K98 model. Finally, we conclude in Sect. 6.

2. Zodiacal light modelling

ZL is commonly modelled sample-by-sample in time-domain by performing line-of-sight integration at each observation through a parametric three-dimensional model of the IPD distribution. We adopt the same general parametrization as introduced by K98 for the current `Commander3` implementation, and in this section we briefly review the main aspects of this model, aiming to build intuition about the underlying parametric model. We also consider a few numerical approximations that reduce the overall computational cost. For full details of this model, we refer the interested reader to Kelsall et al. (1998).

2.1. Parameterization of interplanetary dust

IPD in the zodiacal cloud is overall smooth and stable (Leinert & Pitz 1989), and most of the dust may be accounted for by a diffuse cloud-like component (Kelsall et al. 1998). The origin of IPD is debris mainly from comets (Liou et al. 1995; Ipatov et al. 2008; Rigley & Wyatt 2022), asteroids (Dermott et al. 1984) and meteoroids (Dikarev & Schwarz 2015), with potential additions from planets (Jorgensen et al. 2021), the Kuiper belt (Mann et al. 2009), and interstellar dust passing through the Solar system (Rowan-Robinson & May 2013). The relative contribution to the overall IPD density from these sources is not well known, but many models predict the main source to be low-eccentricity Jupiter family comets that rapidly disintegrate due to frequent trips through the inner Solar system. Within the mostly smooth zodiacal cloud, fine structures exist near the Ecliptic plane as a result of collisions and fragmentation in the asteroid belt and gravitational resonance and disturbance in the orbit of the planets (Low et al. 1984; Dermott et al. 1984, 1994; Reach et al. 1997). There are also structures found in the orbits of other solar system planets, (Kennedy et al. 2011; Jones et al. 2013; Stenborg et al. 2018), but these are potential extensions to the Kelsall model.

We model the IPD distribution as a combination of several zodiacal components, each described by a number density $n_c(x, y, z)$, where c indicates components and x, y and z indicate heliocentric Ecliptic coordinates. Each zodiacal component is allowed to have a heliocentric offset $(x_{0,c}, y_{0,c}, z_{0,c})$, such that the component-centric coordinates become

$$\begin{aligned} x_c &= x - x_{0,c} \\ y_c &= y - y_{0,c} \\ z_c &= z - z_{0,c}. \end{aligned} \tag{1}$$

Additionally, each zodiacal component is allowed to have a plane of symmetry that is different from the Ecliptic, which is defined by an inclination i_c and an ascending node Ω_c . Components that happen to be azimuthally symmetric are then fully described by a radial distance r_c from the origin and the height

above the symmetry plane Z_c ,

$$r_c = \sqrt{x_c^2 + y_c^2 + z_c^2}, \quad (2)$$

$$Z_c = x_c \sin \Omega_c \sin i_c - y_c \cos \Omega_c \sin i_c + z_c \cos i_c, \quad (3)$$

$$\zeta_c = \frac{|Z_c|}{r_c}, \quad (4)$$

with ζ_c being the radial height above the symmetry plane.

2.2. Zodiacal components

With these definitions in hand, we now define parametric models for each IPD component type.

2.2.1. Smooth cloud

By far the most important component is typically referred to as the ‘‘zodiacal cloud’’. This component represents the smooth IPD distribution in the inner Solar system. Its number density is modeled as

$$n_C(x, y, z) = n_{0,C} r_C^{-\alpha} f(\zeta_C), \quad (5)$$

where $n_{0,C}$ is the number density at 1 AU, α is a power-law index, $f(\zeta_C)$ is the fan-like vertical distribution given as

$$f(\zeta_C) = \exp[-\beta g(\zeta_C)^\gamma], \quad (6)$$

with

$$g(\zeta_C) = \begin{cases} \zeta_C^2/2\mu & \text{for } \zeta_C < \mu, \\ \zeta_C - \mu/2 & \text{for } \zeta_C \geq \mu, \end{cases} \quad (7)$$

where β , γ and μ are shape parameters.

2.2.2. Dust bands

Next, three dust bands are included in the model to represent the observed shoulder-like structure in the IRAS scans across the ecliptic plane. These bands appear at Ecliptic latitudes of approximately $\pm 1.4^\circ$, $\pm 10^\circ$, and $\pm 15^\circ$, and are associated with a blend of the Themis and Koronis, the Eos, and the Io/Maria asteroid families, respectively (Reach et al. 1997). Each dust band, indicated by B_i , is modeled as

$$n_{B_i}(x, y, z) = \frac{3n_{0,B_i}}{r_{B_i}} \exp\left[-\left(\frac{\zeta_{B_i}}{\delta_{\zeta_{B_i}}}\right)^6\right] \left[1 + \left(\frac{\zeta_{B_i}}{\delta_{\zeta_{B_i}}}\right)^p v^{-1}\right] \quad (8)$$

$$\times \left\{1 - \exp\left[-\left(\frac{r_{B_i}}{\delta_{r_{B_i}}}\right)^{20}\right]\right\}, \quad (9)$$

where n_{0,B_i} is the number density of band B_i at 3 AU, $\delta_{r_{B_i}}$ is the inner radial cut-off, and p , v and $\delta_{\zeta_{B_i}}$ are shape parameters.

2.2.3. Circum-solar ring and Earth-trailing feature

Finally, a circum-solar ring (denoted ‘‘SR’’) component is included in the model to represent dust that has accumulated in Earth’s orbit due to gravitational effects (Dermott et al. 1994). This component also includes an enhancement to the IPD distribution at Earth’s wake, known as the ‘‘Earth-trailing feature’’

(denoted ‘‘TF’’). The composite ring component (denoted ‘‘R’’) is then modeled as

$$n_R(x, y, z, \theta) = n_{0,SR} \exp\left[-\frac{(r_R - r_{0,SR})^2}{\sigma_{R,SR}^2} - \frac{|Z_R|}{\sigma_{Z,SR}}\right] + n_{0,TF} \exp\left[-\frac{(r_R - r_{0,TF})^2}{\sigma_{R,TF}^2} - \frac{|Z_F|}{\sigma_{Z,TF}} - \frac{(\theta - \theta_{0,TF})^2}{\sigma_{\theta,TF}^2}\right], \quad (10)$$

$$(11)$$

where θ is the heliocentric longitude of the Earth, and the radial locations $r_{0,SR}$, $r_{0,TF}$ specify the distances to the peak densities $n_{0,SR}$, $n_{0,TF}$. The σ parameters are length scales for the r , Z and θ parameters, respectively. We note that the Earth-trailing feature depends on the position of the Earth and does not have a plane symmetry like the other zodiacal components.

2.3. Radiative and scattering properties

Equations (5)–(11) define the number density of each component. However, the signal actually measured with an infrared detector is defined by an intensity, I_ν , typically measured in units of MJy sr⁻¹ or nW m⁻² Hz⁻¹ sr⁻¹. The connection between the number density and this thermal emission is modeled in terms of a blackbody modified by an emissivity factor $E_{c,\lambda}$ ¹,

$$I_{c,\lambda}^{\text{Thermal}} = E_{c,\lambda} B_\lambda(T), \quad (12)$$

where B_λ is the Planck function at a wavelength λ (Kelsall et al. 1998). A key parameter in this equation is the IPD temperature T , which is assumed to fall off with radial distance r from the Sun as

$$T(r) = T_0 r^{-\delta}, \quad (13)$$

where T_0 is the temperature of IPD at 1 AU and δ is a power law index which is expected to be ~ 0.5 for grey dust. In addition to emitting thermally, IPD grains also scatter sunlight in near-infrared wavelengths. The contribution to the total signal from scattering reads

$$I_{c,\lambda}^{\text{Scattering}} = A_{c,\lambda} F_\lambda^\odot(r) \Phi_\lambda(\Theta), \quad (14)$$

where $A_{c,\lambda}$ is the albedo (or reflectivity) of the IPD, $F_\lambda^\odot(r)$ the solar flux at a radial distance from the Sun, and $\Phi_\lambda(\Theta)$ is the so-called phase function for scattering angles Θ , which describes the angular distribution of the scattered light (Kelsall et al. 1998).

The total intensity from a single IPD grain is then

$$I_{c,\lambda}^{\text{Total}} = I_{c,\lambda}^{\text{Scattering}} + I_{c,\lambda}^{\text{Thermal}} \quad (15)$$

$$= A_{c,\lambda} F_\lambda^\odot \Phi_\lambda + (1 - A_{c,\lambda}) E_{c,\lambda} B_\lambda, \quad (16)$$

where we have additionally taken into account that reflective material have lower thermal emission by adding a factor $(1 - A_{c,\lambda})$ to the thermal term. The total ZL signal may then be evaluated by summing up the intensity from all dust grains, which in practice means evaluating a line-of-sight integral for each observation,

$$I_{p,t,\lambda} = \sum_c \int n_c \left[A_{c,\lambda} F_\lambda^\odot \Phi_\lambda + (1 - A_{c,\lambda}) E_{c,\lambda} B_\lambda \right] ds. \quad (17)$$

¹ In these expressions, λ denotes wavelength channel, and may be referred interchangeably to both the physical wavelength and the DIRBE channel ID, e.g., channel 1 corresponds to 1.25 μm ; see Hauser et al. (1998) for a full definition.

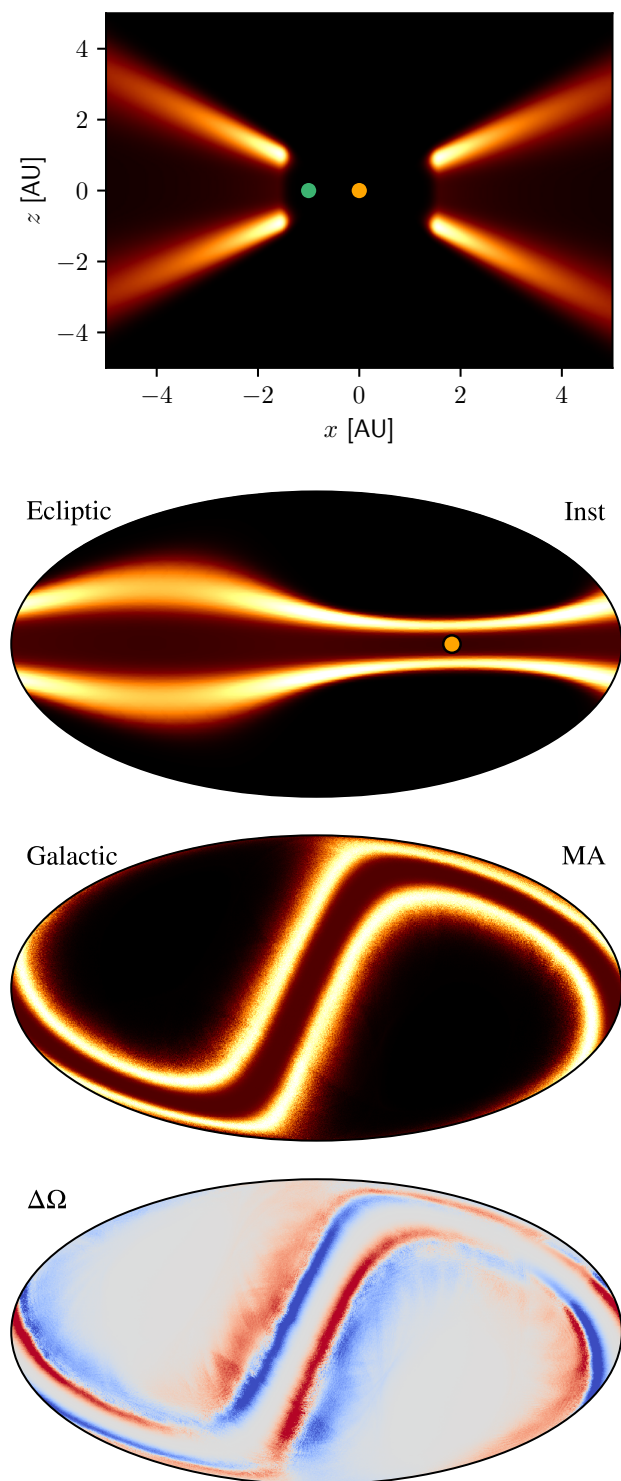


Fig. 1. Geometry of the third asteroidal dust band. (*First row:*) Slice through the x - z plane of the number density, n_0 , in heliocentric coordinates. The positions of the Sun and Earth are marked by orange and green dots, respectively. (*Second panel:*) Observed instantaneous intensity plotted in Ecliptic coordinates, obtained by integrating the above figure along each line-of-sight. (*Third row:*) Same as above, but plotted in Galactic coordinates and mission averaged (MA) over nearly a full year of observations corresponding to the DIRBE scanning strategy. (*Fourth row:*) Normalized difference between observed intensities as defined in the third row after changing the value of the ascending node, Ω , by 5%. Similar plots for all components and parameters are provided in Appendices A and B.

Here, p represents an observed pixel or direction in the sky, t is the time of observation; n_c is the number density of component c in the line-of-sight; and ds is a small distance along the line-of-sight s from the observer and towards p .

Due to the limited signal-to-noise ratios, we follow Kelsall et al. (1998) and only fit one overall albedo for each high-frequency channel, as well as only one common emissivity for all three asteroidal bands. However, unlike in the original K98 analysis, we allow a non-zero albedo for the $4.9\ \mu\text{m}$ channel.

2.4. Model intuition

As described above, the K98 model has only $O(10^2)$ free parameters, which we collectively denote ζ_z . Clearly, this is in reality far too few to fully capture the true complex nature of ZL across many decades in wavelength. However, even with such a limited number of parameters, the model is still severely under-constrained when fitted to the DIRBE data, and the corresponding posterior distribution exhibits many strong degeneracies. Consequently, most currently available parameter estimation algorithms are prone to getting trapped in local posterior maxima, and this then will result in significant residuals in the final ZL cleaned maps.

In order to interpret such residuals, and potentially define better starting points for the non-linear optimization algorithm, it is useful to build up human visual intuition regarding the impact of each free parameter. Figure 1 shows one specific (and arbitrary) example of this. First, the top panel shows a x - z -plane slice through the three-dimensional IPD number density distribution for the third dust band, B_3 . In this figure, the orange dot marks the Sun's position, while the green dot marks the observer's (or Earth's) position. Here it is worth noting that this component is azimuthally symmetric about the Sun, and the full 3D structure may therefore be visualized by rotating this figure about the vertical z -axis. In this space, it is quite straightforward to visualize the effect of each free parameter defined by Eq. (9). For instance, the position of the inner radial cut-off can be changed by modifying δ_r , while the angle between the x -axis and the peak densities may be changed through δ_ζ . If we modify the x_0 offset, the entire density field will shift left or right.

The second panel in Fig. 1 shows the corresponding signal in Ecliptic coordinates at one single point in time after integrating the density field along each line-of-sight. The Sun's position is again marked by an orange dot, but in this case there is obviously no observer position, since this figure shows the sky as seen outwards from the observer. In this projected 2D space, the observed structures appear significantly more difficult to visualize than in 3D space. For instance, while the density of the dust bands appear symmetric in 3D space, their apparent separation and width as seen from Earth vary significantly with Ecliptic longitude, as seen in the second panel; they appear narrower when looking towards the Sun, where the bands are physically further away from the Earth, and broader closeby.

The third panel shows the same feature, but now averaged over nearly a whole year of observations, corresponding to the DIRBE scanning strategy, and plotted in Galactic coordinates. This represents the signal seen in full-mission maps derived from DIRBE. Since the underlying IPD structure is azimuthally symmetric about the Sun, the Earth's movement throughout the year also symmetrizes the total co-added signal, and the dust bands once again appear symmetric about the Ecliptic plane. However, some small-scale structures also appear because of small variations in the effective scanning path of the instrument from day to day; if an entire day's worth of observations were missing, for

instance due to a period of excessive cosmic ray radiation, strong stripes would appear in this map.

With the infrastructure for computing such full-mission maps ready at hand, we can study the impact of each free parameter in greater detail. As a specific example of this, the bottom panel in Fig. 1 shows the normalized difference between the total signal obtained when changing the ascending node Ω for Band 3 by 5% relative to the base model. Intuitively, this corresponds to rotating the signal in the top figure slightly about the origin. Some parts of the bands will then appear closer to the Earth, while others will appear further away. Those regions then in turn appear either red or blue in the bottom figure. The resulting pattern is a unique signature for Ω , and if similar structures are observed in the final ZL cleaned maps, then one should consider modifying this particular parameter in a future analysis.

Similar figures are provided for all components and all parameters in Appendices A and B, and these are very useful for building up visual intuition regarding the K98 model. Quickly scanning through the individual panels in Figs. B.1 and B.2, we can already now identify strong degeneracies that are likely to turn out problematic later. For instance, we see that $n_{0,C}$, α_C , $n_{0,SR}$, T_0 , and δ are all dominated by a ring centered along the Ecliptic plane, and these are likely to interplay significantly. Furthermore, many of these parameters, such as $n_{0,C}$, $\sigma_{z,SR}$, and $\sigma_{\theta,TF}$, will obviously also couple significantly to a wide range of non-ZL type parameters when integrated into a global analysis framework, including the all-important CIB monopoles.

2.5. Numerical optimizations

Performing the line-of-sight integrals defined by Eq. (17) is an expensive part in the COSMOGLOBE DR2 analysis pipeline already for the DIRBE data, which only comprise 18 GB after compression. In principle, this could be done by brute-force for this particular experiment on modern computer clusters, but such a direct approach will clearly not be an option for similar analyses of *Planck* HFI, AKARI and SPHEREx.

When sampling parameters for the ZL model it is possible to include only a small fraction of the full dataset in each likelihood evaluation, simply because the signal-to-noise ratio of each sample is so high, and because of the smooth ZL gradient of the ZL structure. Intuitively speaking, white instrumental noise is irrelevant compared to overall systematic model uncertainties, and some number of consecutive time-domain samples therefore provide essentially the precisely same information. In our current analysis, we adopt a thinning factor of eight, meaning that we effectively fit the data to a time-stream sampled at 1 Hz rather than the original 8 Hz DIRBE CIO. In principle, we could have averaged over this time segment, rather than simply omitting the relevant samples, in order to suppress instrumental noise; and, in fact, the first implementation of our computer code did exactly this. However, averaging over 1 sec time scales implies that the true underlying model is also smoothed out the same time scales, and this increases the overall modeling errors. Although the differences were generally small, we obtained slightly better fits by thinning rather than averaging.

A second optimization step is introduced by dividing the parameters in ζ_z into a set of so-called sampling groups, and estimating the free parameters in each group separately. Specifically, it is worth noting that the overall signal-to-noise ratio for the ZL component shape parameters, such as Ω_C or δ , is vastly dominated by the 12 and 25 μm channels. At the same time, the emissivity and albedo for a given channel depends only on that same channel, and it is therefore not necessary to process, say,

the 1.25 μm TOD when estimating the 4.9 μm albedo. In practice, we therefore first estimate all ZL shape parameters (and the corresponding emissivities, albedos and monopoles) using only the 12 and 25 μm channels, and then we estimate the emissivity, albedo, and monopole for each of the remaining channels separately — but now conditionally on the shape parameters derived from 12 and 25 μm . The cost of this approach is slightly higher statistical uncertainties on the shape parameters, since the other channels could have contributed with some information for these parameters as well, but the gain is a computational speed-up of roughly one order-of-magnitude, and we consider this an excellent trade-off.

3. Methods

The main operational goal of this paper is to measure the free ZL parameters, ζ_z , using time-ordered data from the DIRBE instrument. However, these data contain many other physical effects in the form of both instrumental and astrophysical confusion (e.g., Hauser et al. 1998; Arendt et al. 1998). In order to estimate ζ_z robustly, it is essential to account for all those other degrees of freedom at the same time. On the other hand, many of those parameters have only a limited signal-to-noise ratio with DIRBE data alone, and far stronger constraints will typically result from combining the DIRBE measurements with external data. Enabling such global multi-experiment analysis is a main goal of the COSMOGLOBE framework (Gerakakis et al. 2023). In this section, we briefly review the key ideas behind this approach, and we describe the generalizations that are required for ZL parameter estimation. For full details, we refer the interested reader to Watts et al. (2023, 2024a). However, we emphasize that the approach presented here is only a first step, and future work should aim at implementing faster and more robust algorithms.

3.1. Data model, posterior distribution, and Gibbs sampling

The first step in many Bayesian parameter estimation methods is to write down an explicit parametric data model. For COSMOGLOBE DR2, we adopt the following model,

$$\mathbf{d} = \text{GB} \left[\mathbf{P} \sum_{c=1}^{n_{\text{comp}}} \mathbf{M}_c \mathbf{a}_c + \mathbf{s}_{\text{zodi}} + \mathbf{s}_{\text{static}} \right] + \mathbf{n}, \quad (18)$$

$$\equiv \mathbf{s}^{\text{tot}} + \mathbf{n}, \quad (19)$$

where \mathbf{d} denote observed data; \mathbf{G} denotes an overall calibration factor; \mathbf{P} and \mathbf{B} represent the instrumental pointing and beam, respectively; the sum over components c represents the contribution from astrophysical components (thermal dust, free-free, starlight emission etc.), each described by an overall amplitude (which may be a pixelized map) and a mixing matrix, \mathbf{M} , which depends on some set of unknown SED parameters, β ; and \mathbf{n} denotes instrumental noise. We further define \mathbf{a}_{sky} and β_{sky} to be the set of all astrophysical component amplitudes and spectral parameters, and ξ_n to be the set of all free instrumental noise parameters. We also define $\mathbf{a}_{\text{static}}$ by $\mathbf{s}_{\text{static}} = \mathbf{P}_{\text{sol}} \mathbf{a}_{\text{static}}$, where \mathbf{P}_{sol} is the pointing in solar-centric coordinates. Finally, we denote the set of all free parameters in Eq. (18) by ω , and for a full explicit definition of this parameter set, we refer the interested reader to Watts et al. (2024a). Details regarding the foreground model are provided by Galloway et al. (2024); Gjerløw et al. (2024).

As far as this paper is concerned, the key term is \mathbf{s}_{zodi} , which is nothing but Eq. (17) evaluated along the line-of-sight defined by the pointing \mathbf{P} . This term depends on ζ_z , and our task in this

paper is to establish an approximation to the marginal posterior distribution, $P(\zeta_z | \mathbf{d})$. One straightforward way of computing this marginal distribution is, perhaps somewhat surprisingly, to first consider the much bigger task of estimating the full joint posterior distribution, $P(\omega | \mathbf{d})$ — which now includes billions of correlated parameters rather than just a hundred. The reason this is a more straightforward problem, computationally speaking, is that the joint distribution has a well-defined and simple analytic expression that it is possible to sample from, while the marginal distribution does not; for early CMB applications of this two-stage approach, see Jewell et al. (2004); Wandelt et al. (2004); Eriksen et al. (2004).

In order for this to work, we have to assume that the instrumental noise, $\mathbf{n} = \mathbf{d} - \mathbf{s}_{\text{tot}}$, is Gaussian, and for most instruments that is an excellent approximation. In that case, we can write the likelihood, $\mathcal{L}(\omega) \equiv P(\mathbf{d} | \omega)$, as

$$-2 \ln \mathcal{L}(\omega) = (\mathbf{d} - \mathbf{s}^{\text{tot}}(\omega))^T \mathbf{N}_w^{-1} (\mathbf{d} - \mathbf{s}^{\text{tot}}(\omega)) \equiv \chi^2(\omega), \quad (20)$$

and the posterior distribution is then defined by Bayes' theorem,

$$P(\omega | \mathbf{d}) = \frac{P(\mathbf{d} | \omega)P(\omega)}{P(\mathbf{d})} \propto \mathcal{L}(\omega)P(\omega). \quad (21)$$

Here $P(\omega)$ is called the prior, which may be used to inject prior knowledge about given parameters, while $P(\mathbf{d})$ is called the evidence, which for our purposes is just a normalization constant.

In order to map out this full joint posterior, we use a statistical method called Gibbs sampling (e.g., Geman & Geman 1984), which allows us to draw samples iteratively by scanning through all conditional distributions, as opposed to drawing samples directly from the joint distribution. Sampling from N conditional distributions, each defined by a simple analytical distribution, is typically much simpler than drawing from a single joint N -dimensional distribution that does not have a closed form analytical expression. In practice, for the COSMOGLOBE DR2 analysis this translates into the following so-called Gibbs chain:

$$\mathbf{G} \leftarrow P(\mathbf{G} | \mathbf{d}, \xi_n, \beta_{\text{sky}}, \mathbf{a}_{\text{sky}}, \zeta_z, \mathbf{a}_{\text{static}}) \quad (22)$$

$$\xi_n \leftarrow P(\xi_n | \mathbf{d}, \mathbf{G}, \beta_{\text{sky}}, \mathbf{a}_{\text{sky}}, \zeta_z, \mathbf{a}_{\text{static}}) \quad (23)$$

$$\beta_{\text{sky}} \leftarrow P(\beta_{\text{sky}} | \mathbf{d}, \mathbf{G}, \xi_n, \mathbf{a}_{\text{sky}}, \zeta_z, \mathbf{a}_{\text{static}}) \quad (24)$$

$$\mathbf{a}_{\text{sky}} \leftarrow P(\mathbf{a}_{\text{sky}} | \mathbf{d}, \mathbf{G}, \xi_n, \beta_{\text{sky}}, \zeta_z, \mathbf{a}_{\text{static}}) \quad (25)$$

$$\zeta_z \leftarrow P(\zeta_z | \mathbf{d}, \mathbf{G}, \xi_n, \beta_{\text{sky}}, \mathbf{a}_{\text{sky}}, \mathbf{a}_{\text{static}}) \quad (26)$$

$$\mathbf{a}_{\text{static}} \leftarrow P(\mathbf{a}_{\text{static}} | \mathbf{d}, \mathbf{G}, \xi_n, \beta_{\text{sky}}, \mathbf{a}_{\text{sky}}, \zeta_z), \quad (27)$$

where \leftarrow indicates the process of drawing a sample from the distribution on the right-hand side. Each sampling step in this chain is described by Watts et al. (2024a) and references therein — except for Eq. (26), which is the main topic of this paper.

Based on the data model in Eq. (18), we can define the following residual

$$\mathbf{r} = \mathbf{d} - (\text{GPB} \sum_{c=1}^{n_{\text{comp}}} \mathbf{M}_c \mathbf{a}_c + \mathbf{s}_{\text{static}}), \quad (28)$$

and this should ideally only contain ZL and noise. As such, the assumed Gaussianity of the noise also defines the conditional distribution in Eq. (26), and we may write

$$-2 \ln P(\zeta_z | \mathbf{d}, \dots) = \sum_{\nu} \left(\frac{\mathbf{r}_{\nu} - \mathbf{s}_{\nu, \text{zodi}}(\zeta_z)}{\sigma_{\nu}} \right)^2 \equiv \chi^2(\zeta_z), \quad (29)$$

where we have introduced multiple data frequency channels, denoted by ν , and also for simplicity neglected the prior, $P(\zeta_z)$. We

also define the reduced chi-squared $\chi_{\text{red}}^2 = \chi^2/n_{\text{TOD}}$, where n_{TOD} is the number of TOD samples included in the likelihood evaluation. In this framework, ZL parameter estimation is thus nothing but a traditional Gaussian χ^2 optimization (or sampling) problem after all non-ZL contributions have been subtracted from \mathbf{d} . Precisely how we implement this operation in the current pipeline is described in Sect. 3.3.

So far we have silently skipped past one important term in Eq. (18), namely $\mathbf{s}_{\text{static}}$, which is discussed in detail by (Watts et al. 2024a). As noted by Hauser et al. (1998) and Kelsall et al. (1998), the DIRBE TOD contain significant excess radiation that is not well described by the low-dimensional parametric K98 model. Shortly after these observations, Leinert et al. (1998b) showed that some of this radiation appeared to be stationary in solar-centric coordinates; see their Figure 54. Such radiation can in principle be created through several different physical mechanisms. For instance, a yet unknown zodiacal component could create a signal that appears stationary in solar-centric coordinates, just like the circular-solar ring described in Sect. 2.2.3, or it could also be caused by stray-light contamination in the DIRBE optics. However, even though this radiation was first noted more than two decades ago, it was never mapped out systematically until now, as part of the current COSMOGLOBE DR2 analysis (Watts et al. 2024a). For the time being, we choose to remain agnostic regarding the physical origin of this signal, and therefore, strictly speaking, the ZL model presented in the current paper only describes the parts of the total observed ZL that is attributable to the K98 parametrization. In the future, it is possible that the static component presented by Watts et al. (2024a) should also be added to this model. However, before that is done, it is imperative to rule out the stray-light hypothesis, and that will require both detailed modelling of the DIRBE instrument and joint analysis with other experiments, such as AKARI, IRAS, and *Planck* HFI. Doing that is beyond the scope of the current COSMOGLOBE data release, but it will certainly be a main topic for future work.

Related to this, we also note that the circum-solar ring and trailing feature discussed in Sect. 2.2.3 are completely degenerate with a general pixelized static component in solar-centric coordinates, and it is therefore not possible to fit these and the excess radiation component simultaneously. For this reason, we fix the circum-solar ring and trailing feature parameters at their K98 values, and note that these will have to be revisited once a physical model for the excess radiation has been established.

3.2. Comparison with K98 fitting algorithm

Before describing the practical numerical implementation used for sampling from Eq. (26) in this paper, it is worth first considering the more important fundamental differences between our approach and that adopted by the DIRBE team as described by Kelsall et al. (1998). The first difference worth noting in this respect is that while our χ^2 statistic is defined directly in terms of TOD, the K98 parameter estimation method works with weekly maps. That is, the raw data are co-added week-by-week into pixelized maps, and these are fed into a corresponding pixel-based χ^2 statistic. One important motivation for working with weekly maps rather than single TOD samples is lower computational requirements, which was more important two decades ago than it is today.

A second important difference between the two algorithms — and this is conceptually a far more important one — is the fact that while our method makes active use of an explicit parametric data model for all non-ZL components, the K98 algorithm elim-

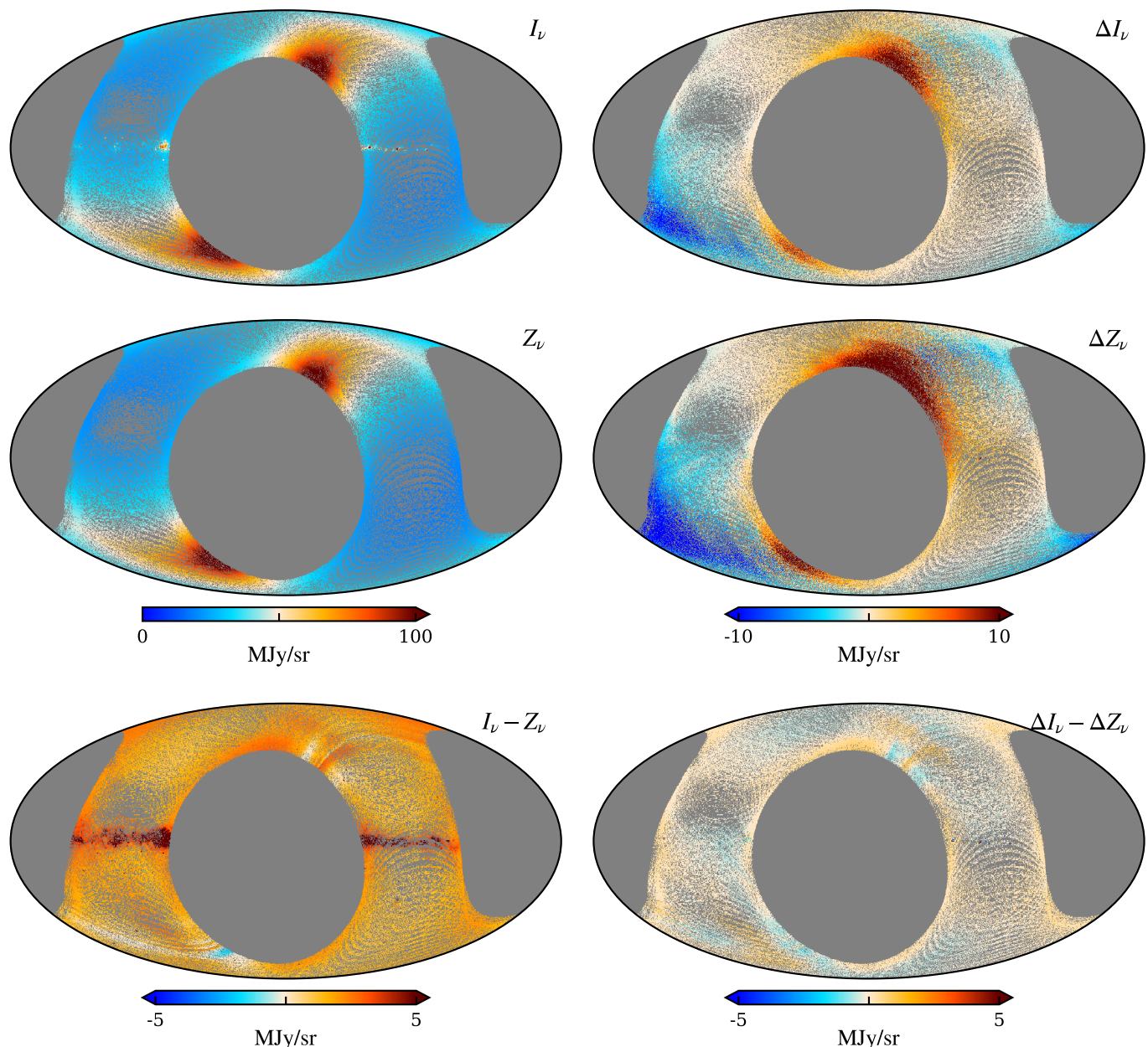


Fig. 2. Illustration of the basic sky maps involved in the ZL fitting algorithms adopted by the K98 (*right column*) and COSMOGLOBE (*left column*) pipelines for one week of $25\ \mu\text{m}$ observations and adopting the K98 model. The K98 pipeline used exclusively differences between weekly and full-season maps, both for the observed signal, $\Delta I_v \equiv I_v - \langle I_v \rangle$ (*top right*), and the ZL model, $\Delta Z_v = Z_v - \langle Z_v \rangle$ (*middle right*), where brackets indicate full-survey averages. Correspondingly, the final χ^2 is defined through $\Delta I_v - \Delta Z_v$ (*bottom right*), and is by construction only sensitive to time-variable signals. In contrast, the basic data element in COSMOGLOBE is the full sky signal, I_v (*top left*), which is fitted with the full ZL model, Z_v (*middle left*), both modelled in time-domain. The χ^2 used in the COSMOGLOBE analysis minimizes the total signal-minus-model residual, $I_v - Z_v$ (*bottom left*). The main advantage of the K98 approach is insensitivity to stationary sky signals, in particular thermal dust and CIB, while the main advantage of the COSMOGLOBE approach is a much higher effective signal-to-noise ratio, both to ZL parameters and zero-levels, as seen by comparing the two bottom panels.

inates any contributions from non-ZL components by only considering differences between weekly maps and the corresponding full-mission average map in their χ^2 statistic. That is, rather than optimizing the full χ^2 as defined in Eq. (29), their algorithm optimizes

$$-2 \ln P_{\text{K98}}(\zeta_z | \mathbf{d}, \dots) = \sum_{i,v} \left(\frac{\Delta \mathbf{d}_{i,v} - \Delta \mathbf{s}_{i,v,\text{zodi}}(\zeta_s)}{\sigma_v} \right)^2 \quad (30)$$

$$\equiv \chi_{\text{K98}}^2(\zeta_z), \quad (31)$$

where i indicate week number, $\Delta \mathbf{d}_{i,v} = \mathbf{d}_{i,v} - \langle \mathbf{d}_{i,v} \rangle$, $\Delta \mathbf{s}_{i,v,\text{zodi}} = \mathbf{s}_{i,v,\text{zodi}} - \langle \mathbf{s}_{i,v,\text{zodi}} \rangle$, and brackets denote averaging over the full mission.

Clearly, this statistic has a key philosophical advantage as compared to the full-signal statistic in Eq. (29): It does not require any assumptions regarding the astrophysical nature of a complicated infrared sky. At least to first order, it is by construction safe against biases from foreground modelling errors. However, this bias immunity also comes at a massive cost in terms of

statistical uncertainties, because it is not only immune to astrophysical bias, but it is also by construction blind to the monopole created when producing mission averaged maps, which can be as bright as 20 MJy/sr at the 25 μ m channel ZL signal, meaning that a lot of signal-to-noise is lost with this approach.

Figure 2 illustrates this difference. The top left panel shows the full intensity signal as analyzed in the COSMOGLOBE algorithm for one single week of 25 μ m observations. The visual imprint is strongly dominated by the ZL features as seen in the total instantaneous ZL view in Appendix. A, aligned with the Ecliptic plane. The right panel show the same after subtracting the full-mission mean; the characteristic cloud pattern has now turned into differential structures that are difficult to interpret visually. The middle row shows the same for the predicted ZL signal, and the bottom row shows the difference between the top and middle rows, which serves as the input to the χ^2 evaluations.

Several points are worth noting in these figures. First of all, we immediately note that the color scale is one order of magnitude narrower in the right column than in the left column; this will translate directly into lower constraining power for the differential approach.

Second, we see that the Galactic plane signal represents a strongly sub-dominant component in the total signal amplitude. Even relatively large errors made in the model assumptions of these will have a very small impact on the overall ZL estimates, and it is also straightforward to mitigate this effect further by masking out any samples that are close known bright Galactic sources; this is fully equivalent to what is done in the CMB field when estimating the CMB power spectrum.

Third, as seen in the bottom panel, the $\chi_{K98}^2(\zeta_z)$ is also by construction entirely blind to the zero-level of the ZL model: The large relative monopole error between the data and the model seen in the bottom right panel is entirely suppressed in the bottom left panel, and there is by construction no way for the differential method to constrain the absolute level ZL monopole. On the one hand, such blindness may certainly be considered to be an algorithmic strength, as indeed argued by Kelsall et al. (1998), given that one of the main goals of the entire DIRBE experiment was to precisely measure the CIB monopole spectrum (Hauser et al. 1998). Nevertheless, the final derived CIB constraints do of course still depend directly on reconstructed ZL monopole, whatever it may be. Intuitively speaking, the differential method aims to measure the ZL monopole using derivatives alone. Whether that task is easier or harder than to establish a sufficiently accurate model of the Milky Way can only be determined by trying both methods, and comparing the results. In addition, it is also worth noting that derivative measurements in general are far more susceptible to systematic biases from any non-Galactic source than absolute intensity measurements. One important example in this respect is optical non-idealities.

3.3. Posterior sampling by non-linear optimization

To complete the algorithm in Sect. 3.1, we still need to specify the details of the algorithm used to draw samples from Eq. (26). A broad range of Bayesian sampling methods can be envisioned used for this purpose, from simple Metropolis-Hastings (MH) accept-reject samplers to various incarnations of Hamiltonian samplers that exploit derivative information. Indeed, our very first implementation employed a simple MH sampler with manually tuned step lengths, and this was used for early model exploration and code testing. However, this approach was quickly abandoned because it, after a short burn-in period, very quickly

got stuck in a local minimum, and all subsequent proposed samples were rejected.

As noted already in Sect. 2, the main challenge with the ZL posterior distribution is a large number of degeneracies. These translate into a highly structured posterior distribution with many local maxima, and it is generally difficult for most iterative non-linear optimization or MCMC methods to map out such parameter spaces efficiently.

The original K98 analysis used a standard Levenberg-Marquardt algorithm to compute the best-fit model. This is a non-linear optimization algorithm that essentially interpolates between a Gauss-Newton and a gradient descent algorithm. As such, that analysis was also susceptible to getting trapped in a local minimum.

In the current paper, we adopt a pragmatic approach to this problem that uses ideas from both the MH and non-linear optimization approaches. The non-linear optimization step is for now performed with a simple Powell search, which uses a series of bi-directional line searches along a set of conjugate directions. The only reason for choosing this method over, say, Levenberg-Marquardt was one of implementational ease; it does not require derivative information.

The algorithm is defined as follows: We start by initializing all free ZL parameters at the K98 model, and run one Powell optimization to reach the nearest local posterior maximum. We then iterate through all non-ZL Gibbs steps, to obtain a new foreground and instrument model given the new ZL model. When returning to the ZL sampler, we add a Gaussian random fluctuation to each ζ_z parameter, which for now is defined by an rms of 1 % of its original value. We then run a new Powell optimization to identify a new local ZL parameter maximum. This new model is then accepted or rejected based on the following Metropolis-like accept probability,

$$a = \min\left(e^{-\frac{1}{2} \frac{\chi_{\text{red,new}}^2 - \chi_{\text{red,old}}^2}{\delta_a}}, 1\right), \quad (32)$$

where δ_a is a tunable parameter that determines the strictness of the rejection criterion. Explicitly, if a proposed ζ_z has a lower reduced chi-squared χ_{red}^2 than the previous sample, it is always accepted; if it has a higher χ_{red}^2 , it is accepted with probability a . We comment below on the reason this definition uses χ_{red}^2 rather than the absolute χ^2 , as well as how we set a .

In practice, many adjustments have been made gradually over the course of many months and hundreds of short individual test runs to the COSMOGLOBE DR2 data selection, analysis masks, and parametric data model. In each case, the new job has been restarted on the previous best-fit solution. This process of slow, gradual and continuously supervised improvements also serves as a safe-guard against nonphysical local posterior maxima, and effectively adds a meta-layer of simulated annealing to the overall algorithm. Typically, the test runs were only run for a few full Gibbs iterations, as in one to ten full samples. Then, once the data and model configuration was considered sufficiently mature for production, a longer run with hundreds of samples distributed over multiple chains were produced.

The overall behaviour of this hybrid MCMC+optimization algorithm is illustrated in Fig. 3, which shows the χ^2 obtained from the first 10⁶ Powell likelihood evaluations in the penultimate analysis run for the 12+25 μ m ZL sampling group; we show the penultimate chain here rather than the final production run to illustrate the burn-in phase. Each discrete jump corresponds to one new main Gibbs iteration, while the smooth descent between two jumps correspond to the Powell search. The

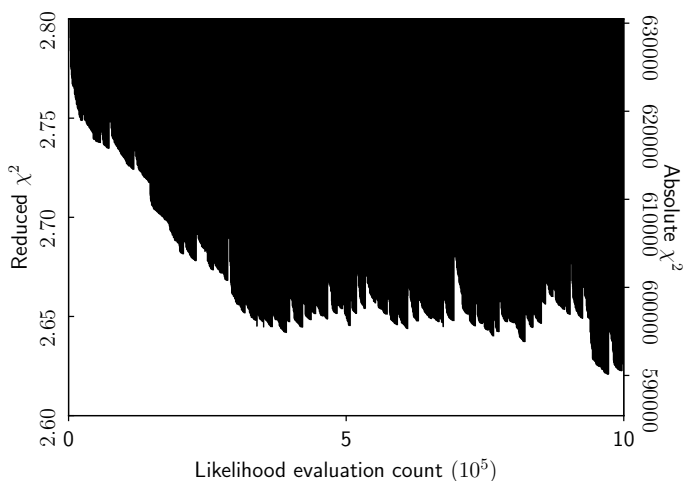


Fig. 3. Reduced χ^2 as a function of Powell likelihood evaluation count for one single pre-production Gibbs chain, showing the burn-in phase. Each discrete jump indicates the start of a new Gibbs sample, which is initialized on a new random point that is close to the previous iteration. The following systematic decline within each main Gibbs iteration indicates the non-linear optimization performed by the Powell algorithm. The solid dark region corresponds to a large number of highly sub-optimal parameter trials.

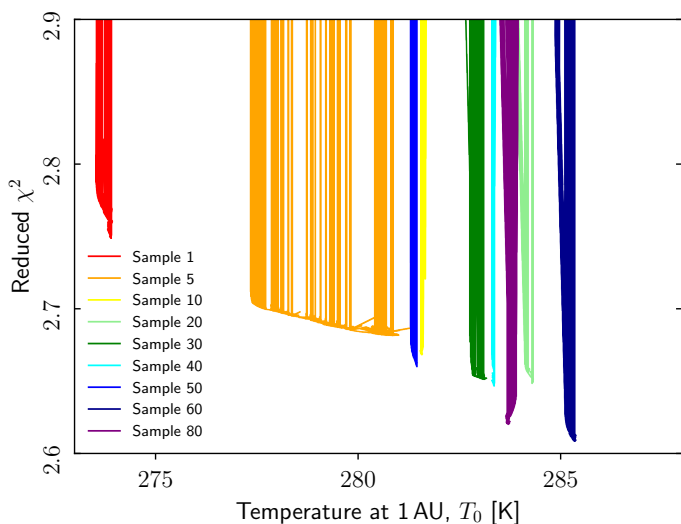


Fig. 4. Reduced χ^2 as a function of the temperature at 1 AU, T_0 for the same run as shown in Fig. 3. Each curve shows the full set of parameter trials within one single Gibbs iteration (or Powell call), and different colors indicate different Gibbs iteration. Redder colors are earlier in the chain.

dense black “roof” corresponds to a large number of very poor parameter estimates made within each Powell search. Only the very last point in each block is propagated forward to the rest of the Gibbs chain. Each likelihood evaluation takes about 0.3 sec wall-time on 128 cores, and the evaluations shown in this figure therefore correspond to about 10 000 CPU-hrs.

We see that the burn-in period appears to be roughly 20 main Gibbs iterations, or about 300 000 likelihood evaluations, after which the chain appears reasonably stationary as measured in terms of χ^2 . As for any MCMC sampler, the chain scatters up and down in χ^2 as it explores the overall parameter space, and sometimes worse models than the previous best-fit are accepted.

Further intuition regarding this pseudo-MH algorithm and the underlying multi-peaked likelihood surface is provided in

Fig. 4, which again shows χ^2_{red} for a large number of likelihood evaluations. However, this time this is plotted as a function of the overall reference temperature of the IPD cloud, T_0 , and also plotted separately for nine individual main Gibbs samples; the sample numbers are color coded according to a rainbow scheme, such that redder colors are closer to the beginning of the Markov chain. Intuitively, the lower edge of each curve represents a snapshot of the local neighborhood around each likelihood minimum. We note that each such likelihood neighborhood is quite sharp, indicating that the optimization algorithm is traversing a rather narrow “likelihood valley”. At the same time, different samples reach a different absolute minimum level that is not a smooth function of T_0 ; this is because of all the other parameters in ζ_z that are effectively marginalized over in this figure. As far as burn-in and convergence is concerned, we see that the Markov chain moves systematically from its initial value at $T_0 \sim 273$ K to ~ 284 K during the first 20 samples, and after that it moves randomly between 282 and 286 K. In sum, this figure illustrates well the highly complex and multi-peaked likelihood surface that must be explored when sampling ZL parameters.

As noted above, we define the accept/reject criterion in terms of a reduced $\chi^2_{\text{red}} \equiv \chi^2/n_{\text{TOD}}$, rather than the absolute χ^2 , as dictated by the traditional Metropolis-Hastings rule. The reason for this is illustrated in Fig. 3, as both the absolute and reduced χ^2 are shown in the right and left y-axes. The point is simply that the main uncertainties in these evaluations is not white instrumental noise, but rather model errors and residual systematics. As far as overall goodness-of-fit is concerned, all models that are derived in the post-burn-in phase appears visually equally good, despite the fact that the absolute χ^2 varies with $O(10^5)$ from model to model. This quantity is therefore a very poor measure for overall acceptability. In contrast, the reduced χ^2 varies with $O(10^{-3})$ from sample to sample, and that is a much more meaningful measure for overall goodness-of-fit. For now, we conservatively set $\delta_a = 0.1$, and the accept probability in Eq. (32) is then primarily a safe-guard against accepting pathologically poor models that lie outside the range seen in Fig. 3.

It is important to stress that this algorithm — because of the random jump proposal rule, the subsequent non-linear optimization phase, and the accept rule based on a reduced χ^2 — does not formally satisfy the mathematical demands to a Monte Carlo Markov Chain sampler in terms of ergodicity or reversibility. It is therefore not guaranteed to converge to the true posterior distribution, even in the limit of an infinite number of samples. Rather, this algorithm is essentially simply a pragmatic solution that allow the previous strict χ^2 optimization algorithm used by Kelsall et al. (1998) to evade local posterior maxima, and explore larger regions of parameter space without getting trapped. Significant additional algorithm development efforts should be invested in establishing efficient methods for this particular posterior distribution.

4. Data

4.1. DIRBE Calibrated Individual Observations

The main data set used in the COSMOGLOBE DR2 analysis is the publicly available DIRBE Calibrated Individual Observations (CIO). These are a user-friendly pre-calibrated version of the raw TOD observed by DIRBE. The CIO are pixelized according to the COBE Quadrilateral cube projection. As part of the data pre-processing, we convert these to corresponding HEALPix pixel indices and re-order them into a time-ordered format. We note that the COSMOGLOBE DR2 maps are binned with $7' \times 7'$ pixels,

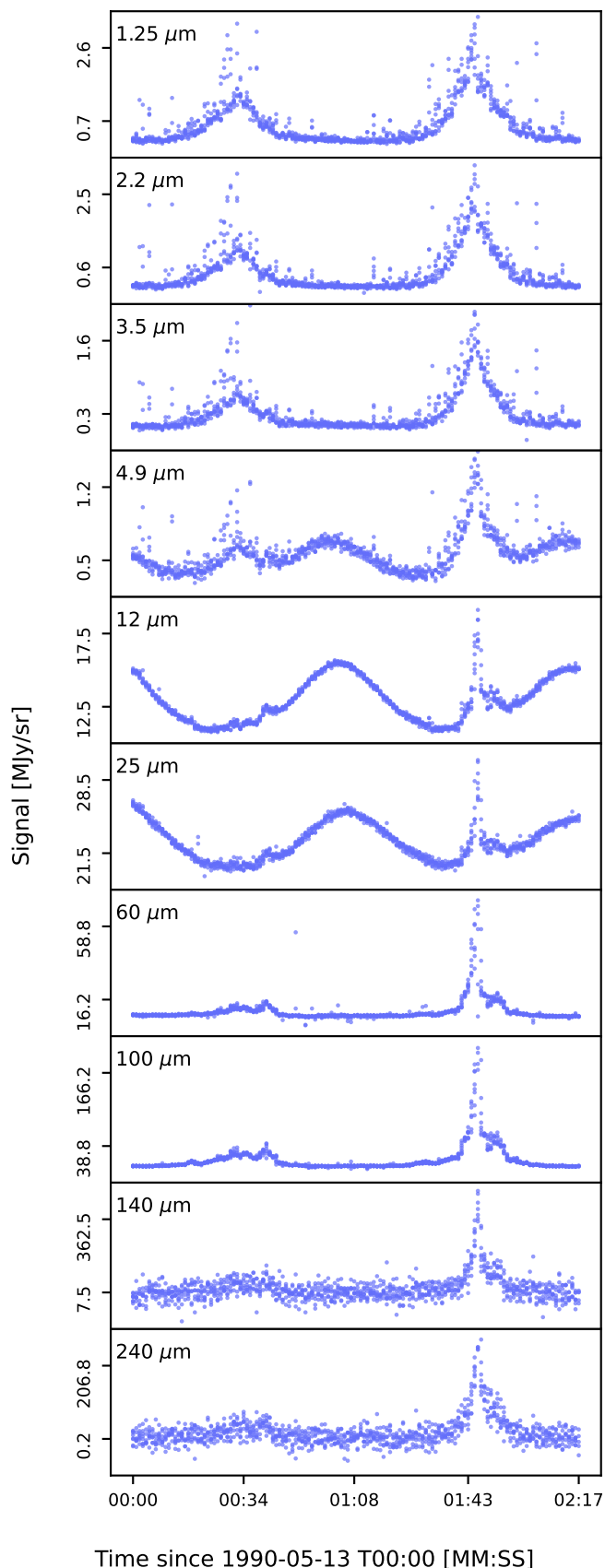


Fig. 5. Subsample of the pre-processed TOD used in this analysis for all ten DIRBE bands. The time-streams show approximately one rotation of the *COBE* satellite which includes two crossing of the Galactic and Ecliptic planes.

corresponding to a HEALPix resolution of $N_{\text{side}} = 512$, which is substantially higher resolution than the pixel size of $19' \times 19'$ used in the original DIRBE analysis. For full details on the pre-processing of the DIRBE CIO we refer to [Watts et al. \(2024a\)](#).

As already noted by [Kelsall et al. \(1998\)](#), a sharp edge may be seen in the K98 ZSMA $25 \mu\text{m}$ map at Galactic coordinates $(l, b) \sim (190^\circ, 15^\circ)$. This corresponds to the very end of the DIRBE observing period. [Watts et al. \(2024a\)](#) studies this effect in greater detail, and we find that this artefact may be mitigated by omitting the last two weeks for the $1.25\text{--}3.5 \mu\text{m}$ channels, and the last month for the $4.9\text{--}100 \mu\text{m}$ channels. A similar sharp feature may be detected near the start of the survey as well, and we therefore also remove the first week observations in all ten frequency channels. Other features that could be handled in a future release include comet trails, which have been found at the 1% level in the 12 and $25 \mu\text{m}$ bands ([Arendt 2014](#)).

In addition, to minimize the impact of the excess radiation component, [Watts et al. \(2024a\)](#) define a set of masks in solar-centric coordinates for each frequency channel between 1.25 and $100 \mu\text{m}$, and any TOD sample that is excluded by these masks is removed from further analysis. This approach plays exactly the same role as the solar elongation cut used by the DIRBE team to produce their final ZSMA maps, but provides much better precision in terms of removing specific systematic features.

In the following, we will refer to the pre-processed CIO as TOD. A subsample of the TOD for each DIRBE band as used in our analysis can be seen in [Fig. 5](#), where we show data for one rotation of the spacecraft about its boresight. Within this rotation, both the Galactic and Ecliptic planes are crossed twice. The two peaks at around 30 sec and 1 min 45 sec correspond to the Galactic plane crossings, while the sine-like waves in bands 4.9 , 12 , and $25 \mu\text{m}$ are due to the ZL emission which peaks in the Ecliptic plane.

In order to trace seasonal ZL modelling errors, we divide the TOD for each DIRBE channel into two, corresponding to the first and second half of the full survey. All ZL parameters are fitted jointly and simultaneously using all data, but the resulting ZL cleaned TOD are binned separately into two independent half-mission maps, and the corresponding half-mission difference maps therefore provide information about seasonal ZL variations not captured by the model.

4.2. Ancillary data

As summarized by [Eq. \(18\)](#), the COSMOGLOBE DR2 data model includes a wide range of both astrophysical and instrumental parameters. The DIRBE CIO are clearly not able to constrain this model very well on their own, and we therefore include three additional key datasets. For full details, see [Watts et al. \(2024a,b\)](#); [Galloway et al. \(2024\)](#); [Gjerløw et al. \(2024\)](#).

The first ancillary data set is a set of six *Planck* HFI PR4 maps between 100 and 857 GHz. We preprocess each of these by subtracting the *Planck* PR3 Commander CMB temperature anisotropy map ([Planck Collaboration X 2016](#)) and the best-fit COSMOGLOBE DR1 CMB dipole ([Watts et al. 2023](#)); the *Planck* PR3 GNILC CIB fluctuation maps between 353 and 857 GHz ([Planck Collaboration et al. 2016](#)); and the nominal *Planck* PR4 model for time-independent ZL emission ([Planck Collaboration LVII 2020](#)). Each map is processed at its native HEALPix resolution of $N_{\text{side}} = 2048$. The main purpose of including *Planck* HFI is to constrain the morphology of Galactic thermal dust emission.

The second ancillary data set is the ALLWISE ([Wright et al. 2010](#); [Cutri et al. 2013](#)) compact object catalog at $3.5 \mu\text{m}$

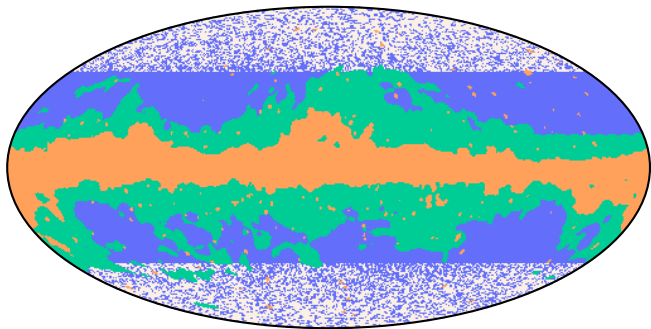


Fig. 6. Three of the processing masks used when estimating ZL parameters. The blue mask is the mask used in the stellar emission dominated 1.25 μm band, the orange mask is used in the ZL dominated 25 μm band, and the green mask is used in the thermal dust dominated 240 μm band.

(denoted W1), which comprise more than 747 million sources. As described by Galloway et al. (2024), the amplitudes of the $\sim 70\,000$ brightest of these sources are fitted source-by-source within the current Commander DR2 Gibbs sampler, while the rest are co-added into a single diffuse model.

The third ancillary data set is *Gaia* DR2?. We attempt to match each source in the AllWISE catalog with *Gaia* DR2, and for those that have a positive match as a star in that catalog (which is more than 90%), we record the effective temperature, T_0 , metallicity, $[M/H]$, and gravitational acceleration, $\log g$; these values are then used to identify the appropriate theoretical stellar SED as provided by the PHOENIX stellar model library (Husser et al. 2013). This spectrum is then convolved with the response function of each DIRBE band between 1.25 and 25 μm , and normalized to unity at 1.25 μm ; only one overall free amplitude is fitted per star in the current analysis. Together, the AllWISE and *Gaia* data provide a state-of-the-art model of starlight emission in the near- and mid-infrared regime.

Finally, a selection of *COBE-FIRAS* (Mather et al. 1994) sky maps are also included in the analysis for monitoring purposes, but they do not contribute with constraining power in the current analysis (Watts et al. 2024a).

4.3. Masks

As discussed in Sect. 3.2, the COSMOGLOBE DR2 parameter estimation algorithm considers the full intensity measured by DIRBE when fitting ζ_z , as opposed to only considering differences between weekly and full-mission maps as Kelsall et al. (1998) did. In order to minimize the risk of confusion from Galactic thermal dust and starlight emission, it is useful to define a confidence mask for each channel that identifies region with a high S/N for ZE, and low S/N for Galactic signals.

For the three channels between 1.25 and 3.5 μm , which are strongly dominated by starlight emission, we generate the ZL confidence mask by thresholding the bright compact source model evaluated at 1.25 μm at 20 kJy/sr. In addition we remove all observations with an absolute Galactic latitude $|b| < 45^\circ$. The resulting mask is shown in blue in Fig. 6, and leaves 18% of the sky available for analysis.

For wavelengths longer than and equal to 60 μm , the starlight emission is negligible, and the Galactic signal is instead dominated by thermal dust emission. At these channels, we therefore instead use the sum of the three thermal dust component maps as the main Galactic tracer. For instance, at 100 μm we threshold

this map at 3 MJy/sr. In addition, we also remove any pixels for which the absolute data-minus-model residual exceeds a given threshold, which for the 100 μm channel was set to 0.8 MJy/sr. The orange and green pixels in Fig. 6 shows the final masks for the 25 and 240 μm channels, which leaves 81 and 52% of the sky available for analysis, respectively.

For the intermediate channels between 4.9 and 25 μm , we threshold on both diffuse and starlight emission. In all cases, we overlay the final masks on the data-minus-model residual map, and verify by eye that no obvious bright Galactic residuals remain after masking.

5. Results

We are now finally ready to present our new ZL model obtained by analyzing the data summarized in Sect. 4 with the algorithm outlined in Sect. 3. We have produced a total of 930 full Gibbs samples, distributed over six Markov chain. We remove the first 20 samples from each chain as burn-in, leaving a total of 810 samples for final analysis. In total, 544 computing cores were used to produce this sample set, for a total cost of about 470k CPU-hrs.

5.1. Markov chains

We start our presentation with a visual inspection of the individual Markov chains for each ZL parameter in ζ_z . These are shown for the general ZL shape parameters in Fig. 7 and for the amplitude (emissivity and albedo) parameters in Fig. 8.² The gray regions indicate the discarded burn-in. Note that we are not attempting to fit the geometrical parameters of dust band 3, but only its number density. Throughout our many attempts, we found that we were unable to constrain the signal in this particular dust band with the DIRBE data alone, as the band would completely disperse.

Examining the trace plots helps to evaluate the degree of convergence for individual parameters. Starting with the shape parameters for the dominant cloud component shown in the left-most column in Fig. 7, we see that many parameters appear to drift slightly during the first 20 samples or so, but after that, they appear more stationary. We also see that the mixing between different chains is notably slower than what is common for most Monte Carlo methods discussed in the literature, and this indicates rather long correlation lengths. Future algorithm development work will aim at decreasing these correlations lengths through better sampling algorithms, as well as reducing the cost per Monte Carlo sample, such that longer Markov chains can be produced. Still, even with the currently available limited sample set, it does appear possible to derive sensible estimates of both the posterior mean and standard deviation for most parameters. It should be noted that the initial value for these parameters are the best-fit parameters of previous trial runs and not the final K98 parameters.

From the component-wise offsets (x_0, y_0, z_0) , we see that the x_0 parameters all appear to have hit the prior limits of ± 0.02 AU,

² Due to a parameter file error introduced before the final production run, the emissivity for asteroidal bands for the 25 μm band, $E_{6,B}$, was accidentally fixed at the best-fit value derived in the penultimate run. This parameter is thus not marginalized over in the current results, but rather fixed at a reasonable value, similar to the parameters that are fixed at their K98 values. The signal-to-noise ratio of the asteroidal bands is, however, very low, accounting only for a few percent of the total ZL signal, and neglecting the uncertainties in this particular parameter has therefore a very small impact on other results.

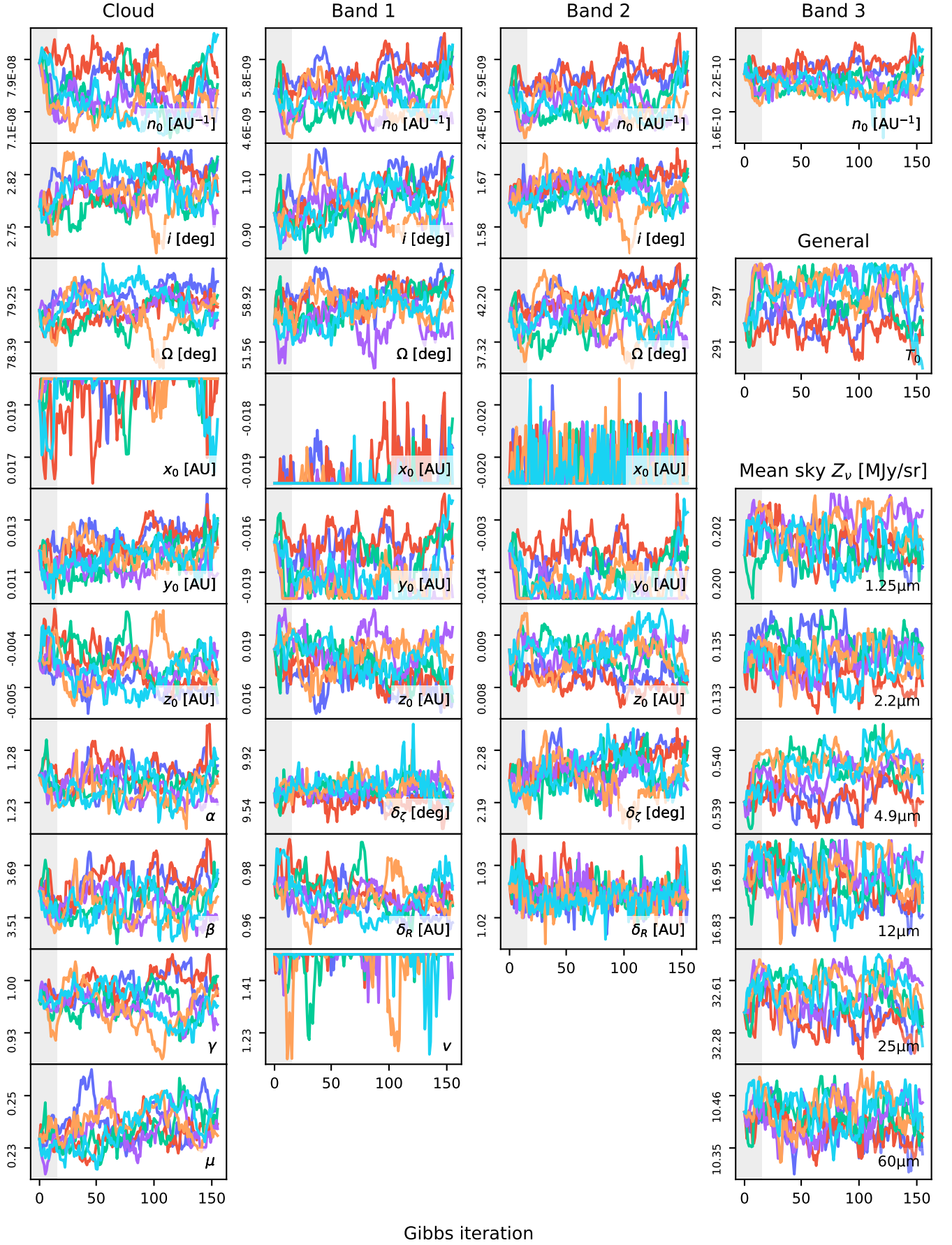


Fig. 7. Trace plots of all geometrical and shape IPD parameters in addition to the IPD temperature at 1 AU T_0 and the full-sky averaged ZL intensity traces for six selected DIRBE channels. The different colors indicate six independent Markov chains, and the gray regions indicate burn-in.

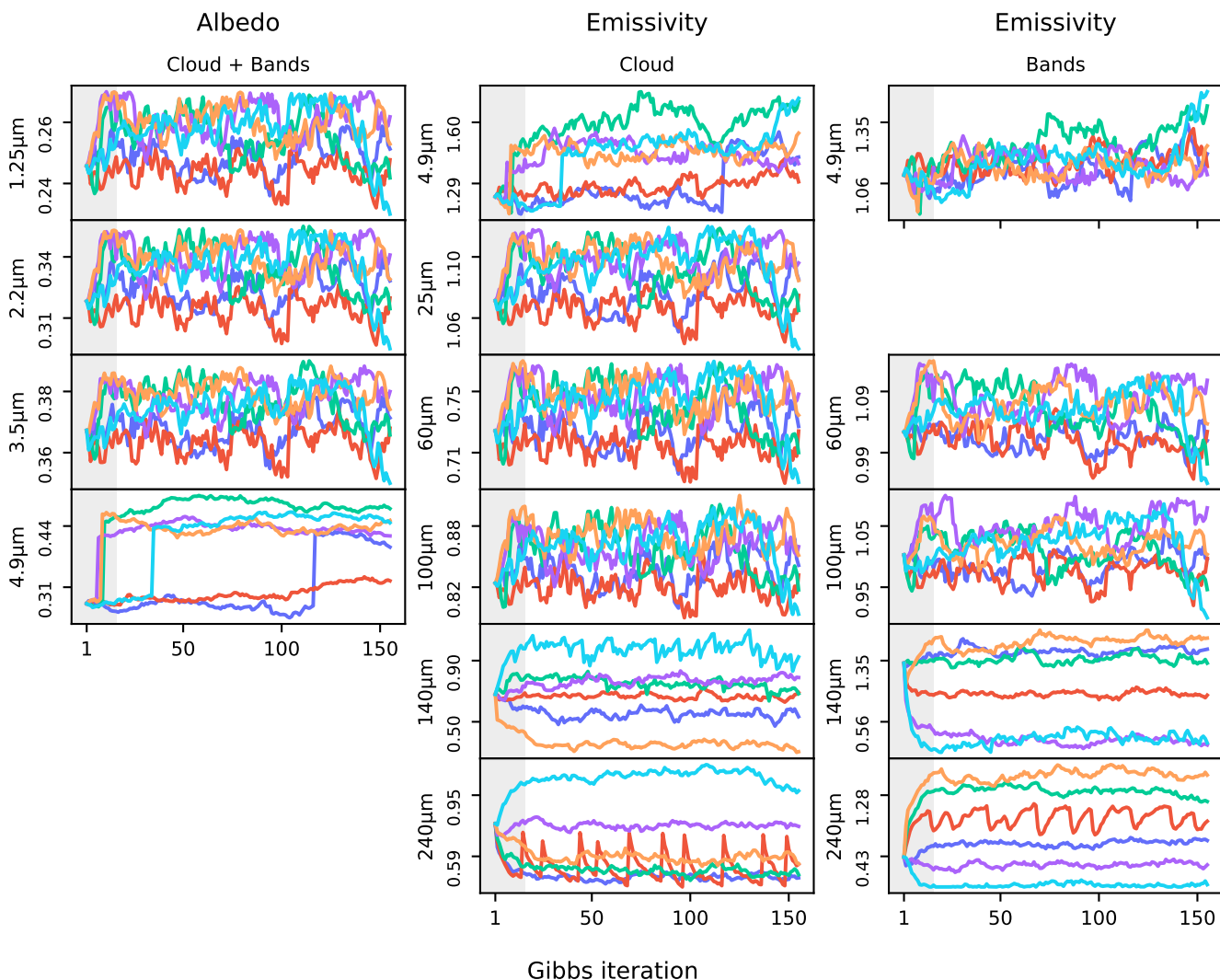


Fig. 8. Trace plots of the wavelength dependent emissivity and albedo parameters. The different colors indicate six independent Markov chains, and the gray regions indicate burn-in.

and the y_0 parameters for the dust bands also hit the floor set by the prior.

Regarding the emissivity and albedo parameters shown in Fig. 8, we see much of the same quantitative behaviour, with a slight drift during the first 20 samples, and generally long correlation lengths. For the 140 and 240 μm channels the correlation lengths are extremely long, and each chain only appears to fall down into a local χ^2 minima after initialization, and then explore a very small region around that initial point. For these channels we also observe a number of apparent phase transitions, in which the Markov chains suddenly move from one stationary state to another, most notably in the curve denoted by the red line, which contains oscillatory features in almost every parameter. This behaviour is another manifestation of the complex multi-peaked ZL likelihood surface discussed in Sect. 3.3. Because of the combination of a very low absolute ZL signal-to-noise ratio of the far-infrared DIRBE channels with strong diffuse Galactic thermal dust emission, there are strong degeneracies between the ζ_z and the Galactic model, which are explored rather inefficiently with the current Gibbs sampler. A future implementation of this framework could consider fitting an overall parametric function for the ZL SED that is smooth in

wavelength, rather than free amplitudes at each channel such that these low S/N channels are supported by the stronger ZL channels in the mid-infrared regime. At the same time, the same low signal-to-noise ratios that make it difficult to estimate the precise values of ζ_z for these values also make the very same values less important as far as cosmological or Galactic science is concerned. The ZL emission at these wavelengths is simply very faint, and therefore less important. In addition, we note that only the sum over all ZL components matters for cosmological analysis, not each individual component, and internal degeneracies are therefore of lower overall concern.

Introducing a free non-zero albedo parameter at the 4.9 μm channel also means we are fitting both an emissivity and albedo in this channel. The degeneracies in the two parameters become apparent by the sudden jump in value simultaneously for the emissivity and albedo traces in all but the red chain. In Eq. (17), we see that if the albedo increases, a larger fraction of the thermal emission is removed, and hence, the emissivity must grow to keep the thermal contribution stable.

Figure 9 shows the Pearson correlation coefficient between pairs of parameters in ζ_z , evaluated directly from the post-burn-in Gibbs sample set. This plot is highly structured, the structure

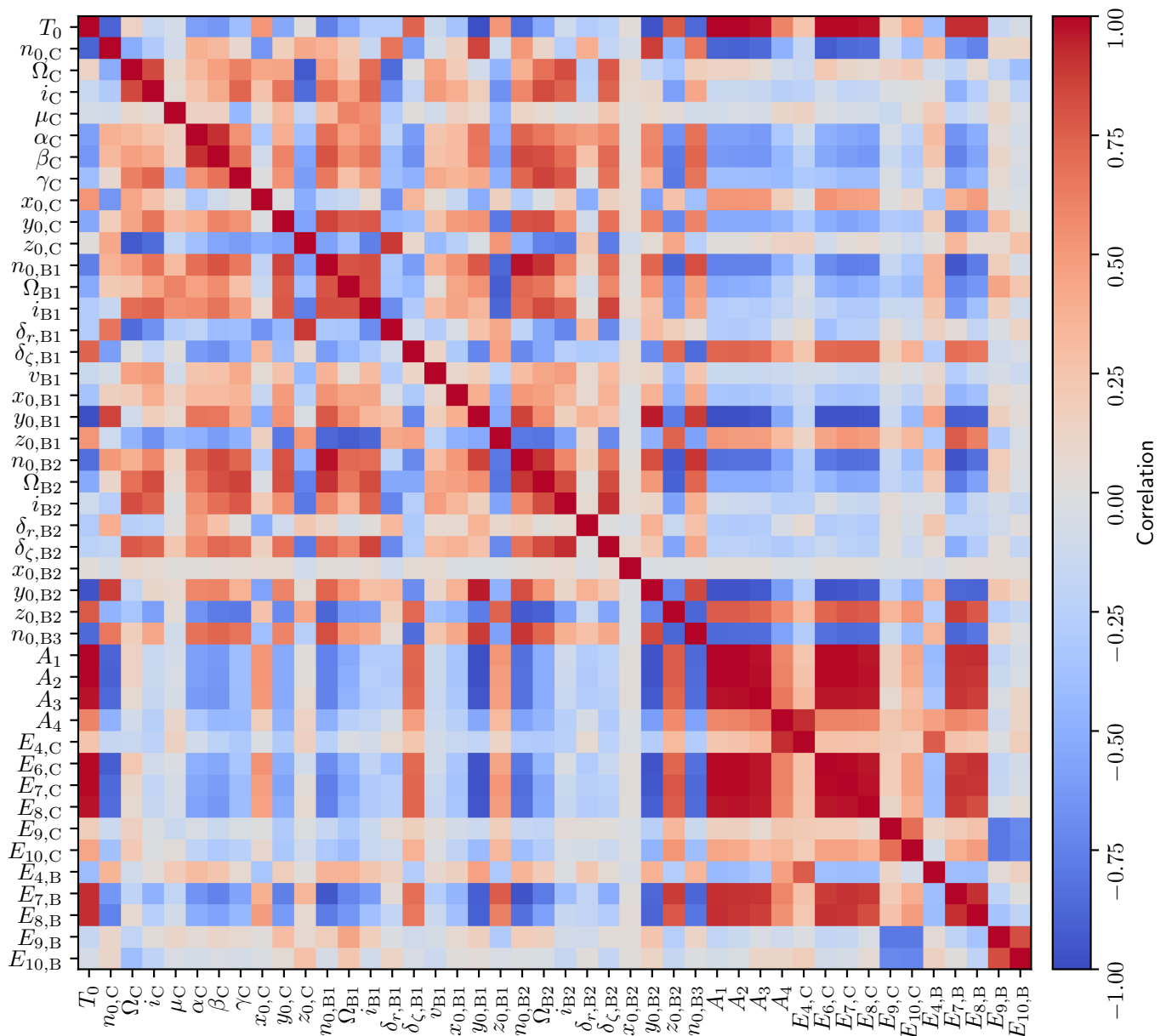


Fig. 9. Correlations between a the fitted ZL parameters ζ_z .

of the complex ZL likelihood. Particularly strong are the correlations between the reference temperature, T_0 , and the emissivity and albedo parameters, E_i and A_i . As already noted above, fitting a smooth parametric ZL SED function rather than individual amplitude factors at each channel should be beneficial in many ways; both in terms of physical interpretation, but also in terms of overall sampling efficiency in a Gibbs sampler. We also see that many of the shape parameters involving the two first asteroidal bands are strongly correlated, and joint analysis with high-resolution experiments such as IRAS and AKARI (Ootsubo et al. 2016; Takahashi et al. 2019) should be highly beneficial in constraining these.

5.2. Updated ZL model

To estimate the marginal posterior distribution for each ZL parameter individually, we compute the mean and standard deviation of all post-burn-in samples. The resulting values for the

shape parameters are tabulated in the third column of Table 1, while the amplitude parameters are provided in Table 2. For comparison, the corresponding values from Kelsall et al. (1998) are listed in the second column in each table. The fourth and final column lists the uniform priors imposed on each parameter in the DR2 analysis.

In general, we see that the differences between DR2 and K98 vary for many parameters more than predicted by the reported statistical uncertainties. For instance, the density of the dominant cloud parameter is about 33% lower in the DR2 model than in K98. At the same time, we also notice that the amplitude of the first band is 10 times higher in the DR2 model than in the K98 model, which accounts for a significant fraction of the lower cloud intensity. In addition, the temperature at 1 AU T_0 has increased from 286K to 294 ± 2 K, which significantly increases the intensity of the ZL light and almost perfectly compensates for the changes in the number densities.

Table 1. Best-fit interplanetary dust parameter estimates and uncertainties in the DR2 analysis, comparing values with the K98 model. Parameters that are not listed are fixed at the respective K98 values. The entry listed with zero uncertainty, ν_{B_2} , has converged to the boundary of the uniform prior listed in the fifth column.

| Parameter | Description | K98 | DR2 | Uniform prior |
|---------------------------------------|-----------------------------|-------------------|-------------------|---------------|
| Smooth Cloud | | | | |
| $n_{0,C}$ [10^{-8} AU $^{-1}$] | Number density at 1 AU | 11.3 ± 0.1 | 7.46 ± 0.26 | [0.001, 100] |
| α | Radial power-law exponent | 1.34 ± 0.02 | 1.25 ± 0.01 | [1, 2] |
| β | Vertical shape parameter | 4.14 ± 0.07 | 3.62 ± 0.05 | [3, 5] |
| γ | Vertical power-law exponent | 0.94 ± 0.03 | 0.99 ± 0.02 | [0.3, 1.1] |
| μ | Widening parameter | 0.189 ± 0.014 | 0.24 ± 0.01 | [0.1, 0.4] |
| i [deg] | Inclination | 2.03 ± 0.02 | 2.82 ± 0.02 | [-30, 30] |
| Ω [deg] | Ascending node | 77.7 ± 0.6 | 79.2 ± 0.2 | [-720, 720] |
| x_0 [10^{-2} AU] | x-offset from the Sun | 1.2 ± 0.1 | 1.98 ± 0.03 | [-2, 2] |
| y_0 [10^{-2} AU] | y-offset from the Sun | 0.55 ± 0.8 | 1.22 ± 0.05 | [-2, 2] |
| z_0 [10^{-3} AU] | z-offset from the Sun | -2.2 ± 0.4 | -4.97 ± 0.26 | [-20, 20] |
| Dust band 1 | | | | |
| n_{0,B_1} [10^{-9} AU $^{-1}$] | Number density at 1 AU | 0.56 ± 0.07 | 5.5 ± 0.3 | [0.001, 100] |
| $\delta_{\epsilon_{B_1}}$ [deg] | Shape parameter | 8.78 Fixed | 9.59 ± 0.05 | [0, 30] |
| ν_{B_1} | Shape parameter | 0.10 Fixed | 1.498 ± 0.009 | [0.01, 2.5] |
| i_{B_1} [deg] | Inclination | 0.56 Fixed | 1.06 ± 0.07 | [-30, 30] |
| Ω_{B_1} [deg] | Ascending node | 80 Fixed | 58.82 ± 1.80 | [-720, 720] |
| $\delta_{R_{B_1}}$ [AU] | Inner radial cutoff | 1.5 Fixed | 0.962 ± 0.005 | [0.8, 5.4] |
| x_0 [10^{-2} AU] | x-offset from the Sun | | -1.97 ± 0.04 | [-2, 2] |
| y_0 [10^{-2} AU] | y-offset from the Sun | | -1.74 ± 0.09 | [-2, 2] |
| z_0 [10^{-2} AU] | z-offset from the Sun | | 1.64 ± 0.07 | [-2, 2] |
| Dust band 2 | | | | |
| n_{0,B_2} [10^{-9} AU $^{-1}$] | Number density at 1 AU | 1.99 ± 0.13 | 2.73 ± 0.10 | [0.02, 100] |
| $\delta_{\epsilon_{B_2}}$ [deg] | Shape parameter | 1.99 Fixed | 2.27 ± 0.02 | [0, 30] |
| ν_{B_2} | Shape parameter | 0.9 Fixed | 0.9 Fixed | Fixed |
| i_{B_2} [deg] | Inclination | 1.2 Fixed | 1.65 ± 0.02 | [-30, 30] |
| Ω_{B_2} [deg] | Ascending node | 30.3 Fixed | 41.78 ± 1.25 | [-720, 720] |
| $\delta_{R_{B_2}}$ [AU] | Inner radial cutoff | 0.94 ± 0.03 | 1.024 ± 0.002 | [0.8, 5.4] |
| x_0 [10^{-2} AU] | x-offset from the Sun | | -2 ± 0.0 | [-2, 2] |
| y_0 [10^{-2} AU] | y-offset from the Sun | | -1.16 ± 0.33 | [-2, 2] |
| z_0 [10^{-3} AU] | z-offset from the Sun | | 8.3 ± 0.2 | [-20, 20] |
| Dust band 3 | | | | |
| n_{0,B_3} [10^{-10} AU $^{-1}$] | Number density at 1 AU | 1.4 ± 0.2 | 2.11 ± 0.09 | [0.1, 10] |

Figure A.3 in Appendix A compares the mission-averaged ZL maps for both models per component. Here we see visually that the DR2 cloud is fainter than the K98 cloud, while all of the bands are brighter. In particular, the first asteroidal band is very faint in K98. In the DR2 model, this component has instead turned into a broad band aligned with the Ecliptic plane, located close to the Earth at its nearest point. In the alternative model presented by Rowan-Robinson & May (2013), the K98 parametrization is replaced by a fan-plus-comet composite. At a

purely visual level, our B_1 component appears to play a similar role as their so-called “broad band” (bb) component.

Figure 10 compares the predicted ZL intensity as a function of wavelength for three different positions on the sky at one given day in different colors, as well as the average over the full sky in black. Solid and dashed lines show the DR2 and K98 predictions, respectively. The bottom panel show the relative difference. In general, the two models agree to better than 10 % for most wavelengths, except at the very longest, for which the

Table 2. Best-fit source function parameter estimates and uncertainties in the DR2 analysis, comparing values with the K98 model. Parameters that are not listed are fixed at the respective K98 values.

| Parameter | Description | K98 | DR2 | Uniform prior |
|-------------------------|---------------------------------|----------------------------|------------------|---------------|
| All zodiacal components | | | | |
| T_0 (K)... | IPD temperature at 1 AU | 286 Fixed | 294 ± 2 | [250, 300] |
| A_1 | Albedo at $1.25\mu\text{m}$ | 0.204 ± 0.001 | 0.25 ± 0.006 | [0, 1] |
| A_2 | Albedo at $2.2\mu\text{m}$ | 0.255 ± 0.002 | 0.32 ± 0.008 | [0, 1] |
| A_3 | Albedo at $3.5\mu\text{m}$ | 0.21 ± 0.02 | 0.37 ± 0.005 | [0, 1] |
| A_4 | Albedo at $4.9\mu\text{m}$ | 0 Fixed | 0.31 ± 0.08 | [0, 1] |
| Smooth Cloud | | | | |
| E_1 | Emissivity at $1.25\mu\text{m}$ | 1 Fixed | 1 | Fixed |
| E_2 | Emissivity at $2.2\mu\text{m}$ | 1 Fixed | 1 | Fixed |
| E_3 | Emissivity at $3.5\mu\text{m}$ | 1.7 ± 0.1 | 1 | Fixed |
| E_4 | Emissivity at $4.9\mu\text{m}$ | 0.997 ± 0.004 | 1.3 ± 0.1 | [0, 5] |
| E_5 | Emissivity at $12\mu\text{m}$ | 0.958 ± 0.003 | 1 | Fixed |
| E_6 | Emissivity at $25\mu\text{m}$ | 1 Fixed | 1.08 ± 0.01 | [0, 5] |
| E_7 | Emissivity at $60\mu\text{m}$ | 0.733 ± 0.006 | 0.72 ± 0.01 | [0, 5] |
| E_8 | Emissivity at $100\mu\text{m}$ | 0.647 ± 0.012 | 0.84 ± 0.02 | [0, 5] |
| E_9 | Emissivity at $140\mu\text{m}$ | 0.677 | 0.55 ± 0.03 | [0, 5] |
| E_{10} | Emissivity at $240\mu\text{m}$ | 0.519 | 0.47 ± 0.02 | [0, 5] |
| Dust bands | | | | |
| E_1 | Emissivity at $1.25\mu\text{m}$ | 1 Fixed | 1 | Fixed |
| E_2 | Emissivity at $2.2\mu\text{m}$ | 1 Fixed | 1 | Fixed |
| E_3 | Emissivity at $3.5\mu\text{m}$ | 1.66 Fixed to smooth cloud | 1 | Fixed |
| E_4 | Emissivity at $4.9\mu\text{m}$ | 0.36 ± 0.05 | 1.13 ± 0.08 | [0, 5] |
| E_5 | Emissivity at $12\mu\text{m}$ | 1.0 ± 0.2 | 1 | Fixed |
| E_6 | Emissivity at $25\mu\text{m}$ | 1 Fixed | 1.01 | Fixed |
| E_7 | Emissivity at $60\mu\text{m}$ | 1.3 ± 0.3 | 1.00 ± 0.02 | [0, 5] |
| E_8 | Emissivity at $100\mu\text{m}$ | 1.5 ± 0.0 | 0.98 ± 0.02 | [0, 5] |
| E_9 | Emissivity at $140\mu\text{m}$ | 1.13 | 1.47 ± 0.05 | [0, 5] |
| E_{10} | Emissivity at $240\mu\text{m}$ | 1.40 | 0.61 ± 0.03 | [0, 5] |

overall amplitudes are very uncertain, and near the $4.9\mu\text{m}$ channel where we have fit a free albedo.

Figure 11 shows a similar relative difference, but now as a function of position on the sky for the 12 and $25\mu\text{m}$ channels. In these channels, for which the ZL emission is the brightest, the K98 and COSMOGLOBE DR2 models agree to within $\lesssim 5\%$ over most of the sky. These differences are thus similar in magnitude to the relative residuals measured by Kelsall et al. (1998), which were found to be $\sim 2\%$ at $12\mu\text{m}$.

5.3. Goodness-of-fit

Next, we consider the absolute goodness-of-fit of the COSMOGLOBE DR2 model, and we start by inspecting the half-mission data-minus-model residual maps for each channel, which are shown in Fig. 12. We note that these maps show total residuals, and therefore include contributions from ZL, Galactic foregrounds, and instrumental noise.

Starting with the near-infrared 1.25 – $3.5\mu\text{m}$ channels, we see that these are primarily dominated by residual starlight emission, seen in the form of the bright Galactic plane and the scattered points source residuals at high Galactic latitudes. However, subdominant contributions from ZL residuals are also clearly seen in the form of diffuse structures aligned with the Ecliptic plane and poles. For instance, in the $1.25\mu\text{m}$ first half-mission map, denoted by HM1, which corresponding to the first five months of the mission, we see a faint band with alternating sign that follows the Ecliptic plane. In fact, similar features may be seen in all channels below $100\mu\text{m}$, and future work should clearly aim at establishing a more detailed model of ZL in the Ecliptic plane; again, joint analysis with high-resolution measurements from IRAS and AKARI should prove extremely useful for this.

In the $1.25\mu\text{m}$ HM1 map, we also see a diffuse excess about 45° south-west of the Galactic center, corresponding to the beginning of the DIRBE observing period. On the opposite side of the missing pixel mask, there is a slight deficit. As noted in

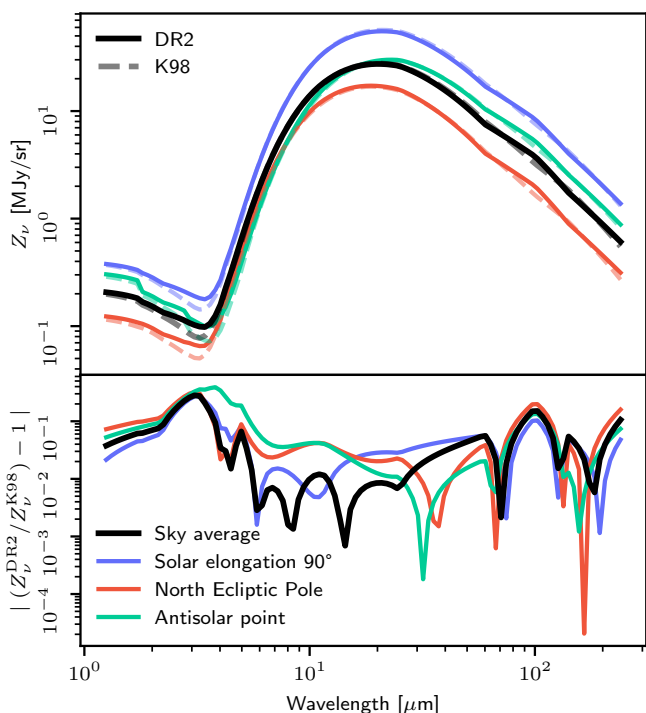


Fig. 10. (Top panel:) ZL intensity as a function of wavelength on the 2024-01-01 as predicted by the DR2 (solid lines) and K98 (dashed lines) models. Colors show three different positions on the sky, and the black curves show the full-sky average. (Bottom:) Fractional difference between the DR2 and 98 models, evaluated from the results shown in the top panel.

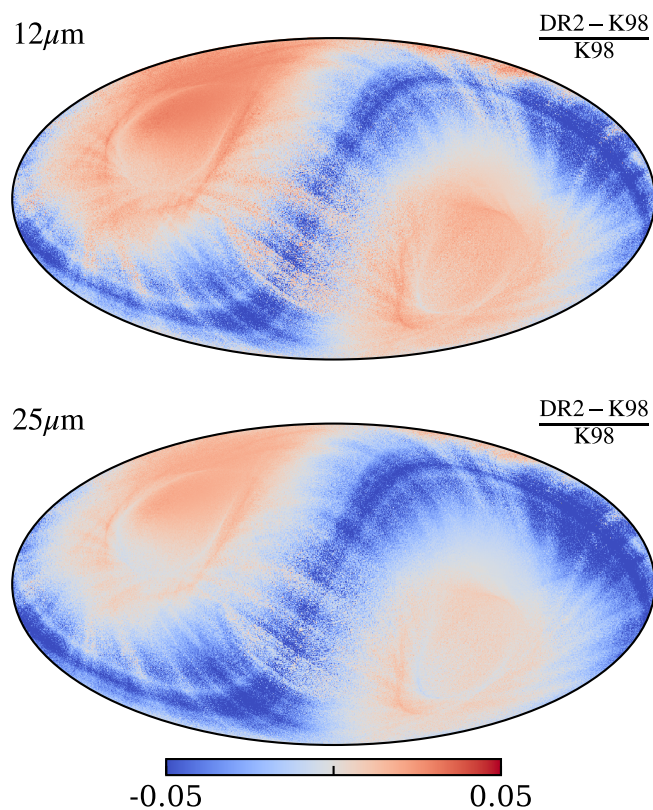


Fig. 11. Relative fractional difference in the mission-averaged ZL simulations at 12 and 25 μm using the K98 model and our best-fit ZL model.

Table 3. Reduced goodness-of-fit (χ_{red}^2) values for one arbitrarily selected Gibbs sample, along with the number of TOD samples used to fit the ZL parameters and the instrument white noise rms per 8 Hz sample for each DIRBE channel. Note that the 12 and 25 μm channels are analyzed jointly, and N_{samp} and χ_{red}^2 correspond to the union of the two.

| λ (μm) | $N_{\text{samp}}(10^3)$ | $\sigma_0[\text{MJy/sr}]$ | χ_{red}^2 |
|-----------------------------|-------------------------|---------------------------|-----------------------|
| 1.25 | 61 | 0.031 | 0.72 |
| 2.2 | 43 | 0.031 | 0.79 |
| 3.5 | 42 | 0.026 | 0.95 |
| 4.9 | 145 | 0.029 | 1.20 |
| 12 | 244 | 0.102 | 3.03 |
| 25 | ... | 0.190 | ... |
| 60 | 120 | 0.322 | 1.62 |
| 100 | 116 | 0.381 | 1.54 |
| 140 | 180 | 32.1 | 1.02 |
| 240 | 170 | 18.3 | 1.03 |

Sect. 4, we remove the first week of observations to suppress this effect. Similarly, in the HM2 map we note that masked pixels correspond to the last two weeks of the mission, and the residuals change sign on each of the two sides of this masked region. In fact, based on these post-analysis residuals, it appears that it might be worth considering removing a few more days at either end of the survey to remove even more of these residuals. Of course, it is impossible to determine from this analysis alone whether these observed residual are due to real ZL variations or instrumental drifts. However, the fact that more than 90% of the survey appears free of sharp edges, and the main features appear either at the end or beginning of the survey suggests at least that an instrumental origin cannot be excluded a priori. For the 4.9–100 μm channels, a whole month is removed at the end of the survey, and a corresponding larger region of missing pixels is seen in HM2.

At 4.9 μm , a peculiar hot band is seen in the south-western quadrant that is close to, but not actually aligned with, the Ecliptic plane. A corresponding blue swath may be seen normal to the Galactic plane in the eastern quadrant. This feature is discussed by Watts et al. (2024a), and shown to correlate directly with a bright feature in excess solar-centric coordinates. Future studies should consider whether this could be explained in terms of stray-light emission, and, if it cannot, then the parametric ZL model for the circum-solar ring and Earth-trailing feature needs to be modified.

Finally, the 100 and 140 μm channels are clearly dominated by Galactic residuals. Any improvement in the ZL model for these channels should therefore be accompanied by corresponding improvements in the thermal dust modelling.

These qualitative observations can be made more quantitative by considering the reduced χ^2 , as optimized within the parameter estimation algorithm. The best-fit χ_{red}^2 values are reported for each channel in the rightmost column of Table 3; note that the 12 and 25 μm channels are processed jointly when fitting the shape parameters, and χ_{red}^2 is therefore only properly defined for the sum of the two. For completeness, the second column lists the number of TOD samples used to fit the ZL parameters, and the third column lists the instrumental white noise rms per TOD sample.

For ideal data, with a perfectly fitting model, we would expect $\chi_{\text{red}}^2 \sim 1$, with a standard deviation given by $\sqrt{2/N_{\text{samp}}} \sim 0.005$. Clearly, the current model is not a perfect match to the observed data, and significant deviations are observed. Still, the

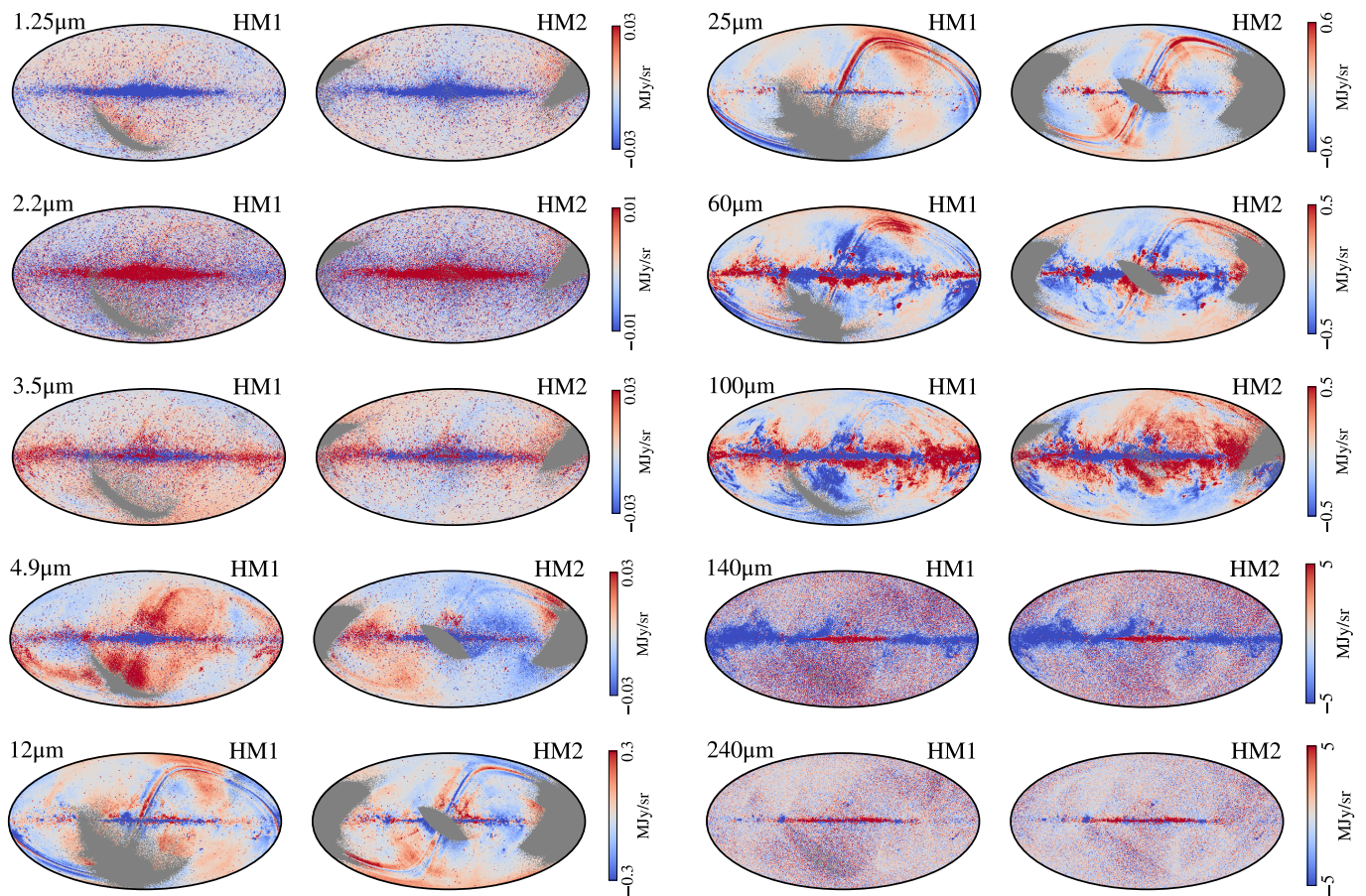


Fig. 12. Half-mission data-minus-signal residual maps for each channel. The two columns within each wavelength section correspond to the first (HM1) and second (HM2) half-mission maps, respectively. All bands between 1.25 and 100 μm have been smoothed with a 15' Gaussian kernel, and the 140 and 240 μm channels have been smoothed with a 30' FWHM kernel. The gray regions represent unobserved pixels in the half-mission splits.

values are for several channels very close to unity, namely 3.5, 140, and 240 μm .

The biggest outliers are the 12 and 25 μm channels, which have the highest signal-to-noise ratio to ZL emission. In this case, the reduced χ^2 is 3.03, which indicates that the white noise rms accounts for only about 40% of the total variation seen in the residual TOD; the rest is most naturally explained in terms of ZL modelling errors. However, in this respect it is worth noting that our estimates of the noise level, as reported by [Watts et al. \(2024a\)](#), are significantly lower than those used for previous ZL analysis with DIRBE observations. For instance, [Rowan-Robinson & May \(2013\)](#) adopted uncertainties of 0.80 and 0.93 MJy/sr per sample at 12 and 25 μm , respectively, which are 8 and 5 times larger than our estimates. Despite assuming such large uncertainties, they obtained a reduced χ^2 of 1.30 with their extended model. In contrast, if we had adopted the same white noise estimates, we would have obtained a reduced χ^2 of ~ 0.1 , which immediately would suggest significant noise rms over-estimation. In other words, the current COSMOGLOBE DR2 analysis has resulted both in significantly lower white noise uncertainties and lower absolute residuals for the main ZL channels.

At the same time, we do in fact obtain reduced χ^2 values that are lower than unity at the two shortest wavelengths. These values suggest that our noise estimates at 1.25 and 2.2 μm are over-estimated by about 15%. The origin of this discrepancy should

be identified and mitigated in future analyses, and it will then be natural to consider the effect of the highly asymmetric beam response of the DIRBE instrument, coupled to the strong starlight emission at these channels. In the current analysis, we assume that the DIRBE beams are azimuthally symmetric ([Watts et al. 2024a](#)), and residuals due to that assumption could presumably easily bias the noise estimates by 15%.

5.4. Comparison of ZSMA maps

A primary goal of the parametric ZL model presented here is to establish a set of zodiacal light subtracted mission averaged (ZSMA) frequency maps for each DIRBE channel that can be used for cosmological and astrophysical analysis. These maps are simply derived by subtracting the ZL component from the TOD, and bin the rest into pixelized sky maps.

Figures 13 and 14 compares the K98 ZSMA maps (second column) with the new COSMOGLOBE DR2 ZSMA maps (third column), as well as with the corresponding non-ZL-subtracted maps (first column). Here we clearly see that the DR2 model results in significantly lower ZL residuals at all channels below 140 μm ; while for the two longest wavelength channels the two maps appear visually very similar. The improvements are particularly striking between 4.9 and 60 μm , where the ZL emission is the strongest. Indeed, the 4.9 and 60 μm channels themselves appear

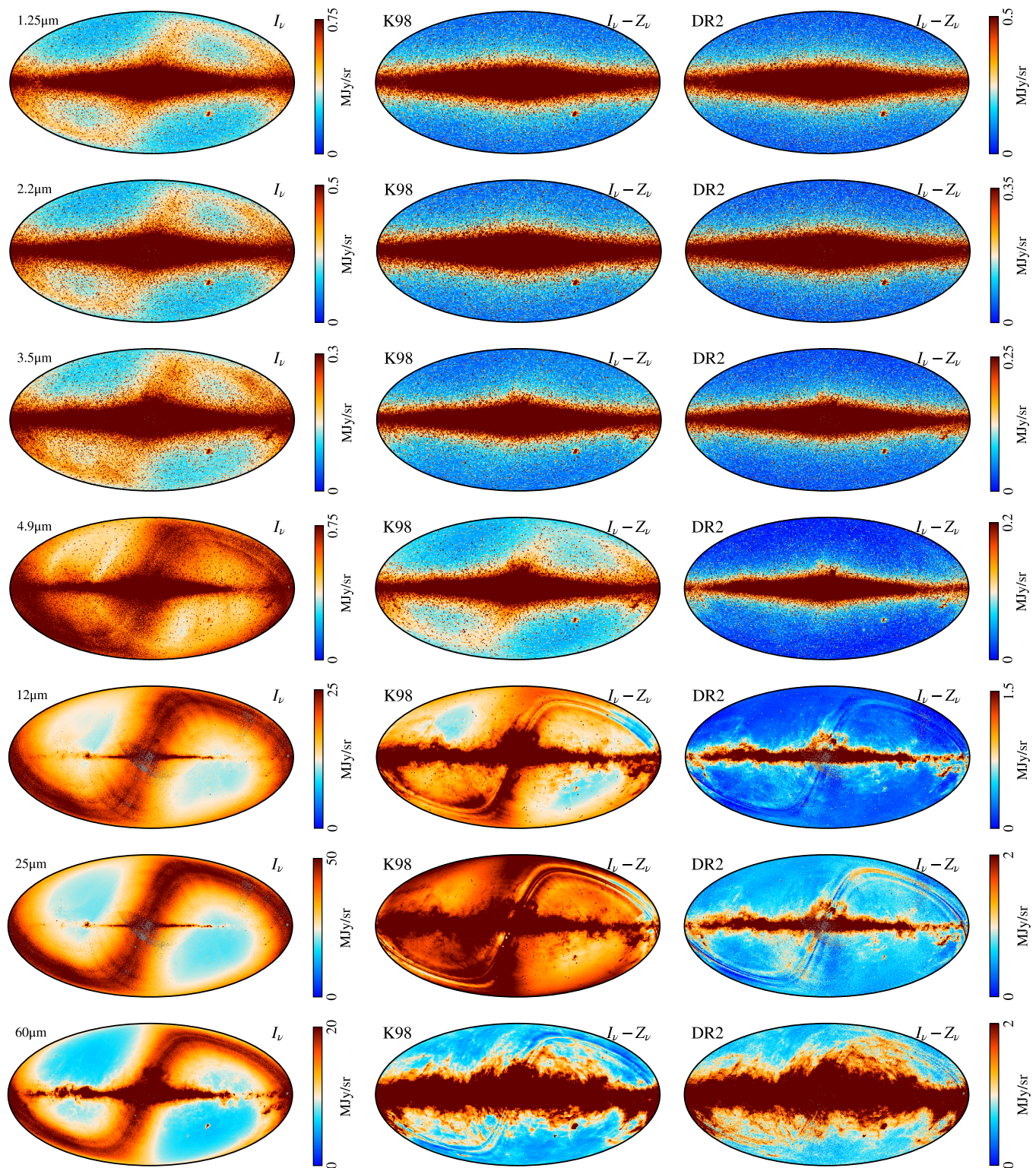


Fig. 13. (Left column): Mission-averaged frequency maps containing ZL after data selection at our native HEALPix resolution of $N_{\text{side}} = 512$. (Middle column): DIRBE ZSMA maps at $N_{\text{side}} = 256$. (right column): Our ZL subtracted mission-average maps, downgraded to $N_{\text{side}} = 256$. Rows show, from top to bottom, DIRBE channels from 1.25 to 60 μm .

for the first time to be dominated by Galactic signal at high latitudes rather than by ZL residuals.

One of the primary scientific goals of the entire DIRBE experiment was to measure the CIB monopole spectrum, which essentially corresponds to the zero-level of the ZSMA maps shown in Figs. 13 and 14. It is therefore of great interest to measure

the difference in zero-levels between the K98 and DR2 maps, shown in Fig. 15 for the 1.25–25 μm channels, evaluated outside the same confidence masks as described in Sect. 4.3. For reference, the best-fit theoretical model of Finke et al. (2022) is plotted as a dotted line. First, we note that the difference is defined as K98-minus-DR2, which is always positive. In other

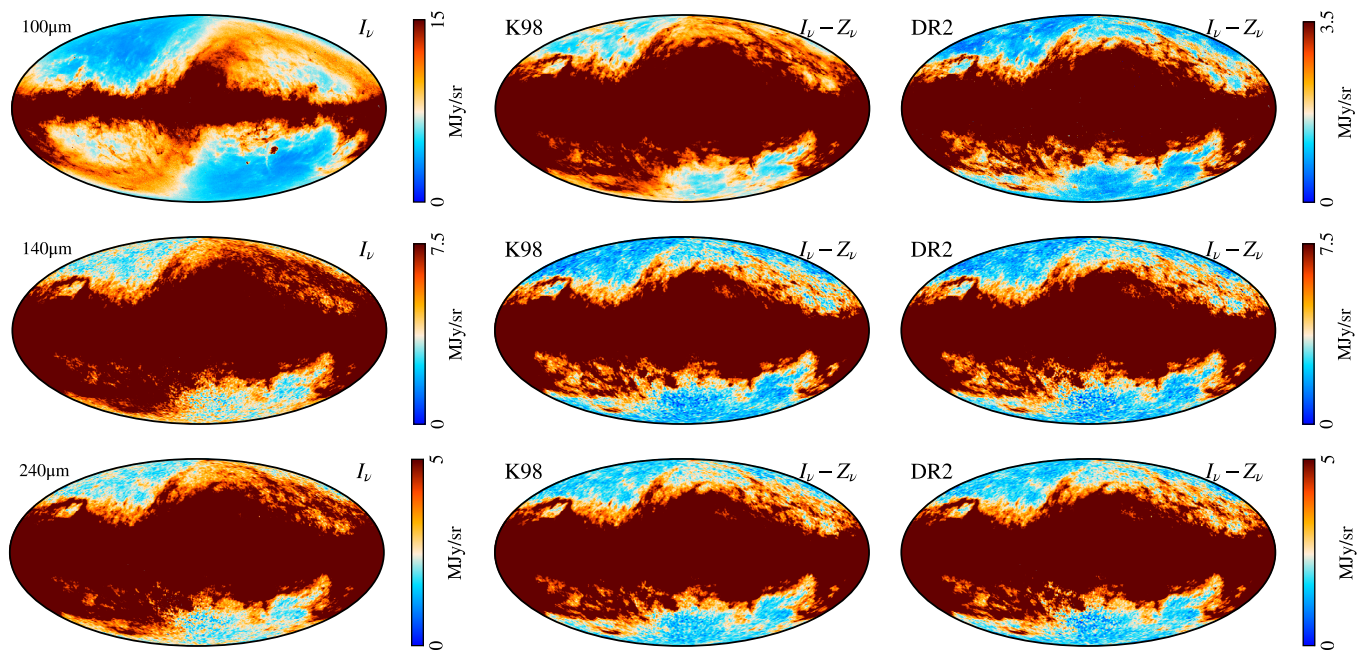


Fig. 14. Same as Fig. 13, but for the 100–240 μm channels.

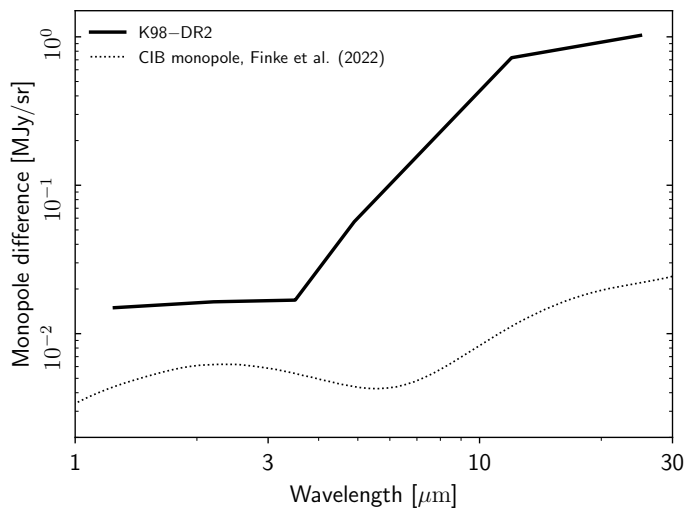


Fig. 15. Monopole difference between official K98 and COSMOGLOBE DR2 ZSMA maps, evaluated as the average of the difference between the maps shown in the second and third columns in Figs. 13 and 14 outside the DR2 analysis masks.

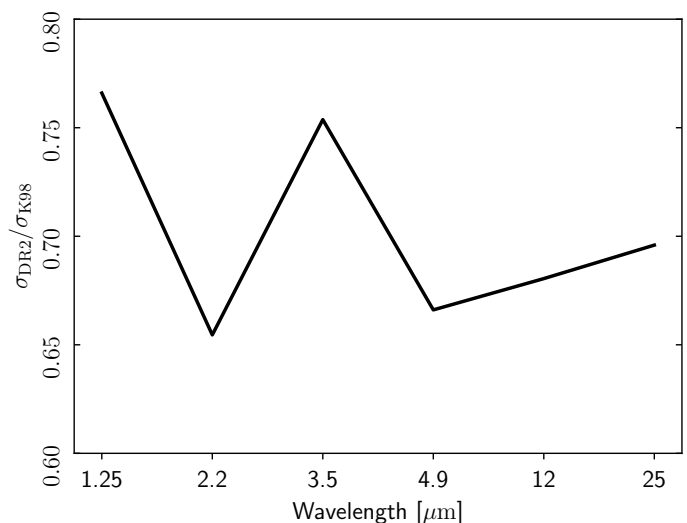


Fig. 16. RMS ratio between the COSMOGLOBE DR2 and K98 ZSMA maps, $\sigma_{\text{DR2}}/\sigma_{\text{K98}}$, as evaluated outside the DR2 analysis masks.

words, the new analysis appears to have removed more ZL than the K98 analysis. In fact, the measured monopole difference is actually also higher than the theoretical CIB monopole spectrum itself, suggesting that the modifications are in fact $O(1)$ or larger as measured relatively to the main science target of DIRBE; at 12 and 25 μm , the differences are almost two orders of magnitude. For further discussion regarding the scientific implications of these differences in terms of the CIB monopole, we refer the interested reader to [Watts et al. \(2024b\)](#).

Figure 16 shows the results from a similar calculations, but this time in the form of the rms ratio of the ZSMA maps evaluated outside the same masks. Here we see that the DR2 maps have $\sim 30\%$ lower rms than the K98 maps, which once again indicates that more ZL emission has been removed from the new maps.

6. Conclusions

We have presented a new Bayesian framework for modelling zodiacal light from time-ordered observations, and applied this to the DIRBE experiment. We find that the resulting ZL model differs significantly from the K98 model, both in terms of mean parameter values and uncertainties, and the new model results in much cleaner ZL-subtracted frequency maps. We strongly recommend that any future cosmological or astrophysical analysis that involves DIRBE frequency maps should use the COSMOGLOBE DR2 maps.

These large improvements stem from two foundational features of the COSMOGLOBE framework. First, the new analysis used external observations from *Planck*, *WISE* and *Gaia* to model Galactic signals, and thereby break, or at least minimize, overall parameter degeneracies. Second, the current framework fits

all parameters simultaneously, both those of astrophysical and instrumental nature. This is achieved through a process called Gibbs sampling, which maps out the full joint posterior distribution by iterating through a large number of conditional distributions.

While this Gibbs sampling approach is a key ingredient in the global process, and it is difficult to envision how the full framework would work without it, this method is also associated with significant numerical challenges. In particular, it is well known that Gibbs sampling struggles with probing strongly degenerate distributions, and the ZL posterior distribution in question in this paper is precisely that. Furthermore, this distribution does not only exhibit strong degeneracies, but also a huge number of local extrema in which a Markov chain can easily get trapped.

Another issue regarding the current model is physical plausibility. In this first application of the Bayesian end-to-end framework, an important goal was to understand how well the current data constrains the parametric model. As a result, only weak uniform priors are imposed on the main fitted parameters. On the one hand, this does ensure that the final residuals are minimized, which is good for astrophysical and cosmological applications of the resulting ZSMA maps – but it also means that some parameters may have likely drifted into non-physical parameter values.

Overcoming all of these challenges will most likely involve at least two main tasks. First, by analyzing additional and complementary data, for instance from high-resolution experiments such as IRAS and AKARI, jointly with the DIRBE measurements, many of the current strong degeneracies are likely to be effectively broken. In particular the structure of the asteroidal bands, for which DIRBE's low angular resolution is a severe limitation, should become much better probed with these data. Still, even with more data there are likely to be several degeneracies present that are difficult to predict in advance. Implementing better and faster sampling algorithms should therefore be a high-priority topic for future work, for instance using ideas from simulated annealing and/or Hamiltonian sampling.

In addition, it is by no means obvious that a low-dimensional 3D model such as K98 with only $O(10^2)$ free parameters can describe such a rich and dynamical system as ZL to the required precision for next-generation cosmology. Future work should therefore also consider conceptual generalizations of the entire framework. One step in this direction was taken by Rowan-Robinson & May (2013), who introduced a different set of basis components than K98; indeed, the new fit presented in this paper appears to have moved toward that model within the K98 framework. More drastic approaches would be to consider perturbative Taylor expansion models around the existing components, or even fully voxelized 3D models. Obviously, these would be highly degenerate when using only near-Earth observations, but perhaps in combination with data from solar system probes such as Juno or New Horizons, new insights may be gained.

In conclusion, it is clear that the ZL model presented in this paper suffers from many shortcomings of both modelling and algorithmic origin, and these must be addressed through future extensions of the COSMOGLOBE framework. At the same time, and despite all these shortcomings, it is equally clear that this model redefines the state-of-the-art of ZL modeling for the DIRBE data, reducing residuals by orders of magnitude in the mid-infrared regime. Furthermore, this work has established an effective computational framework that can be extended to other data sets with relatively minor effort, and that will allow equally large steps forward to be made. All in all, this work has established a new reference for the analysis of past, present and future

infrared experiments, building directly on a long line of algorithmic breakthroughs initially developed for the CMB field.

Acknowledgements. We thank Tony Banday, Johannes Eskilt, Dale Fixsen, Ken Ganga, Paul Goldsmith, Shuji Matsuura, Sven Wedemeyer, and Janet Weiland for useful suggestions and guidance. The current work has received funding from the European Union's Horizon 2020 research and innovation programme under grant agreement numbers 819478 (ERC; COSMOGLOBE), 772253 (ERC; BRIS2COSMOLOGY), and 101007633 (MSCA; CMBINFLATE). Some of the results in this paper have been derived using healpy (Zonca et al. 2019) and the HEALPix (Górski et al. 2005) packages. We acknowledge the use of the Legacy Archive for Microwave Background Data Analysis (LAMBDA), part of the High Energy Astrophysics Science Archive Center (HEASARC). HEASARC/LAMBDA is a service of the Astrophysics Science Division at the NASA Goddard Space Flight Center. This publication makes use of data products from the Wide-field Infrared Survey Explorer, which is a joint project of the University of California, Los Angeles, and the Jet Propulsion Laboratory/California Institute of Technology, funded by the National Aeronautics and Space Administration. This work has made use of data from the European Space Agency (ESA) mission *Gaia* (<https://www.cosmos.esa.int/gaia>), processed by the *Gaia* Data Processing and Analysis Consortium (DPAC, <https://www.cosmos.esa.int/web/gaia/dpac/consortium>). Funding for the DPAC has been provided by national institutions, in particular the institutions participating in the *Gaia* Multilateral Agreement. We acknowledge the use of data provided by the Centre d'Analyse de Données Etendues (CADE), a service of IRAP-UPS/CNRS (<http://cade.irap.omp.eu>, Paradis et al. 2012).

References

- Arendt, R. G. 2014, *AJ*, 148, 135
Arendt, R. G., Odegard, N., Weiland, J. L., et al. 1998, *ApJ*, 508, 74
Bennett, C. L., Larson, D., Weiland, J. L., et al. 2013, *ApJS*, 208, 20
BeyondPlanck Collaboration, Andersen, K. J., Aurlien, R., et al. 2023, *A&A*, 675, A1
Carleton, T., Windhorst, R. A., O'Brien, R., et al. 2022, *AJ*, 164, 170
Cutri, R. M., Wright, E. L., Conrow, T., et al. 2013, Explanatory Supplement to the AllWISE Data Release Products, Explanatory Supplement to the AllWISE Data Release Products, by R. M. Cutri et al.
Dermott, S. F., Jayaraman, S., Xu, Y. L., Gustafson, B. rA. S., & Liou, J. C. 1994, *Nature*, 369, 719
Dermott, S. F., Nicholson, P. D., Burns, J. A., & Houck, J. R. 1984, *Nature*, 312, 505
Dikarev, V. V. & Schwarz, D. J. 2015, *A&A*, 584, A9
Eriksen, H. K., O'Dwyer, I. J., Jewell, J. B., et al. 2004, *ApJS*, 155, 227
Finke, J. D., Ajello, M., Domínguez, A., et al. 2022, *ApJ*, 941, 33
Gaia Collaboration et al. 2016, *A&A*, 595, A1
Galloway, M., Andersen, K. J., Aurlien, R., et al. 2023, *A&A*, 675, A3
Galloway, M., E., G., et al. 2024, *A&A*, in preparation [arXiv:20xx.xxxxx]
Geman, S. & Geman, D. 1984, *IEEE Trans. Pattern Anal. Mach. Intell.*, 6, 721
Gerakakis, S., Brilenkov, M., Ieronymaki, M., et al. 2023, *The Open Journal of Astrophysics*, 6, 10
Gjerløw et al. 2024, *A&A*, in preparation [arXiv:20xx.xxxxx]
Górski, K. M., Hivon, E., Banday, A. J., et al. 2005, *ApJ*, 622, 759
Hauser, M. G., Arendt, R. G., Kelsall, T., et al. 1998, *ApJ*, 508, 25
Hauser, M. G. & Dwek, E. 2001, *ARA&A*, 39, 249
Husser, T. O., Wende-von Berg, S., Dreizler, S., et al. 2013, *A&A*, 553, A6
Ipatov, S. I., Kutyrav, A. S., Madsen, G. J., et al. 2008, *Icarus*, 194, 769
Jewell, J., Levin, S., & Anderson, C. H. 2004, *ApJ*, 609, 1
Jones, M. H., Bewsher, D., & Brown, D. S. 2013, *Science*, 342, 960
Jorgensen, J. L., Benn, M., Connerney, J. E. P., et al. 2021, *Journal of Geophysical Research (Planets)*, 126, e06509
Kelsall, T., Weiland, J. L., Franz, B. A., et al. 1998, *ApJ*, 508, 44
Kennedy, G. M., Wyatt, M. C., Su, K. Y. L., & Stansberry, J. A. 2011, *MNRAS*, 417, 2281
Kornigut, P. M., Kim, M. G., Arai, T., et al. 2022, *ApJ*, 926, 133
Leinert, C., Bowyer, S., Haikala, L. K., et al. 1998a, *A&AS*, 127, 1
Leinert, C., Bowyer, S., Haikala, L. K., et al. 1998b, *A&AS*, 127, 1
Leinert, C. & Pitz, E. 1989, *A&A*, 210, 399
Liou, J. C., Dermott, S. F., & Xu, Y. L. 1995, *Planet. Space Sci.*, 43, 717
Low, F. J., Beintema, D. A., Gautier, T. N., et al. 1984, *ApJ*, 278, L19
Mann, I., Nakamura, A. M., & Mukai, T. 2009, *Small Bodies in Planetary Systems*, Vol. 758
Mather, J. C., Cheng, E. S., Cottingham, D. A., et al. 1994, *ApJ*, 420, 439
Neugebauer, G., Habing, H. J., van Duinen, R., et al. 1984, *ApJ*, 278, L1
Nieto, M. M., Turyshv, S. G., & Anderson, J. D. 2005, *Physics Letters B*, 613, 11
Ootsubo, T., Doi, Y., Takita, S., et al. 2016, *PASJ*, 68, 35
Paradis, D., Dobashi, K., Shimoikura, T., et al. 2012, *A&A*, 543, A103

- Partridge, R. B. & Peebles, P. J. E. 1967, ApJ, 148, 377
- Planck Collaboration, Aghanim, N., Ashdown, M., et al. 2016, A&A, 596, A109
- Planck Collaboration X. 2016, A&A, 594, A10
- Planck Collaboration II. 2020, A&A, 641, A2
- Planck Collaboration III. 2020, A&A, 641, A3
- Planck Collaboration LVII. 2020, A&A, 643, A42
- Poppe, A. R., Lisse, C. M., Piquette, M., et al. 2019, ApJ, 881, L12
- Reach, W. T., Franz, B. A., & Weiland, J. L. 1997, Icarus, 127, 461
- Rigley, J. K. & Wyatt, M. C. 2022, MNRAS, 510, 834
- Rowan-Robinson, M. & May, B. 2013, MNRAS, 429, 2894
- San, M. 2024, Journal of Open Source Software, 9, 6648
- San, M., Herman, D., Erikstad, G. B., Galloway, M., & Watts, D. 2022, A&A, 666, A107
- Sano, K., Matsuura, S., Yomo, K., & Takahashi, A. 2020, ApJ, 901, 112
- Stenborg, G., Stauffer, J. R., & Howard, R. A. 2018, ApJ, 868, 74
- Szalay, J. R., Pokorný, P., Bale, S. D., et al. 2020, ApJS, 246, 27
- Takahashi, A., Ootsubo, T., Matsuhara, H., et al. 2019, PASJ, 71, 110
- Takimoto, K., Arai, T., Matsuura, S., et al. 2022, ApJ, 926, 6
- Takimoto, K., Matsuura, S., Sano, K., & Feder, R. M. 2023, ApJ, 944, 229
- Wandelt, B. D., Larson, D. L., & Lakshminarayanan, A. 2004, Phys. Rev. D, 70, 083511
- Watts, D. et al. 2024a, A&A, in preparation [arXiv:20xx.xxxxx]
- Watts, D. et al. 2024b, A&A, in preparation [arXiv:2406.01491]
- Watts, D. J., Basyrov, A., Eskilt, J. R., et al. 2023, A&A, 679, A143
- Wright, E. L., Eisenhardt, P. R. M., Mainzer, A. K., et al. 2010, AJ, 140, 1868
- Zonca, A., Singer, L., Lenz, D., et al. 2019, Journal of Open Source Software, 4, 1298

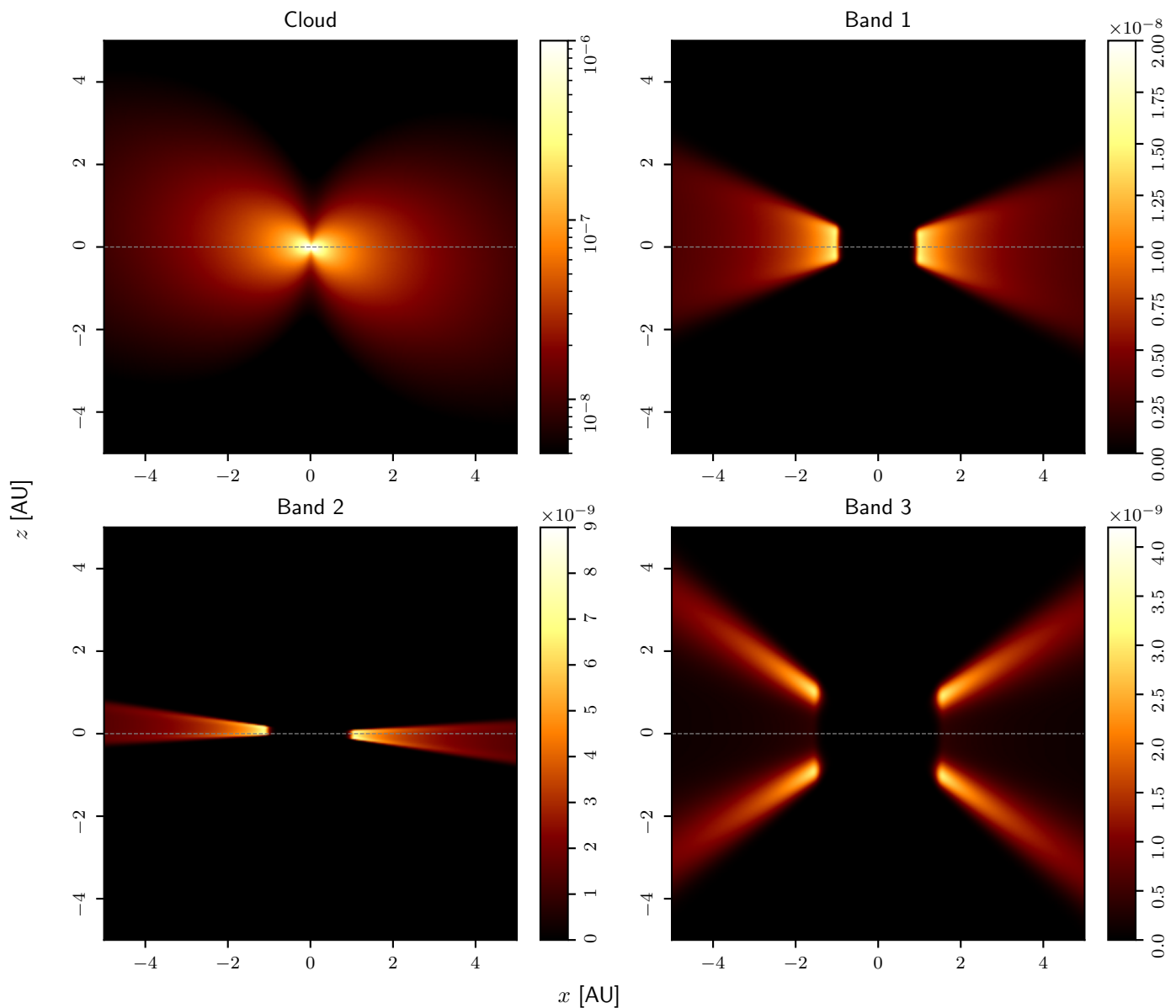


Fig. A.1. Visualization of the IPD number density of the four fitted zodiacal components in our model. The number densities are shown as a cross-section of the Solar system in the xz -plane. (*top left*): The smooth cloud. (*top right*): Dust band 1. (*bottom left*): Dust band 2. (*bottom right*): Dust band 3. The gray dotted line represents the ecliptic plane and helps illustrate the variations in the components symmetry planes.

Appendix A: Component-wise zodiacal light maps and number density cross-sections

In this Appendix we present maps visualizing of our best-fit ZL model. These figures can help illustrate the physical properties of the model and help validate how physical our models are. The ZL component-wise maps, both the mission-averaged and the instantaneous maps in A.3 and A.2, respectively, are compared to the K98 model. The IPD number density visualization for the K98 model, corresponding to Fig. A.1 can be seen in figure 1 and 2 in San et al. (2022).

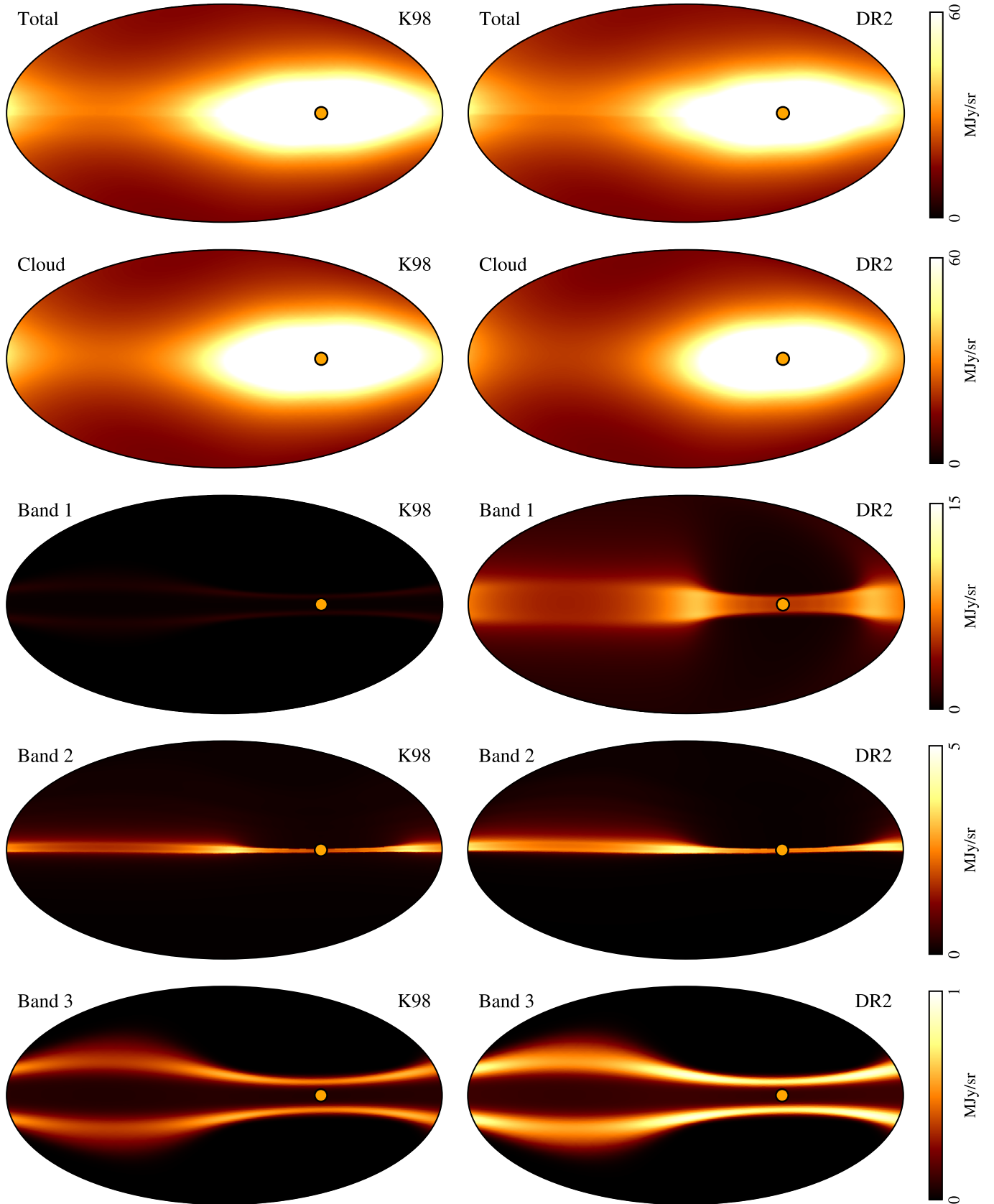


Fig. A.2. Full-sky total and component-wise ZL maps (January 1, 2024) at $25\mu\text{m}$ made with ZodiPy. (*Left column:*) The K98 model. (*Right column:*) Best-fit Cosmoglobe ZL model. Rows list the zodiacal components, from top to bottom, 1) total ZL emission, including the circum-solar ring and Earth-trailing feature; 2) smooth cloud; 3) dust band 1; 4) dust band 2; 5) dust band 3. The maps are in Ecliptic coordinates, with the Sun marked as an orange circle.

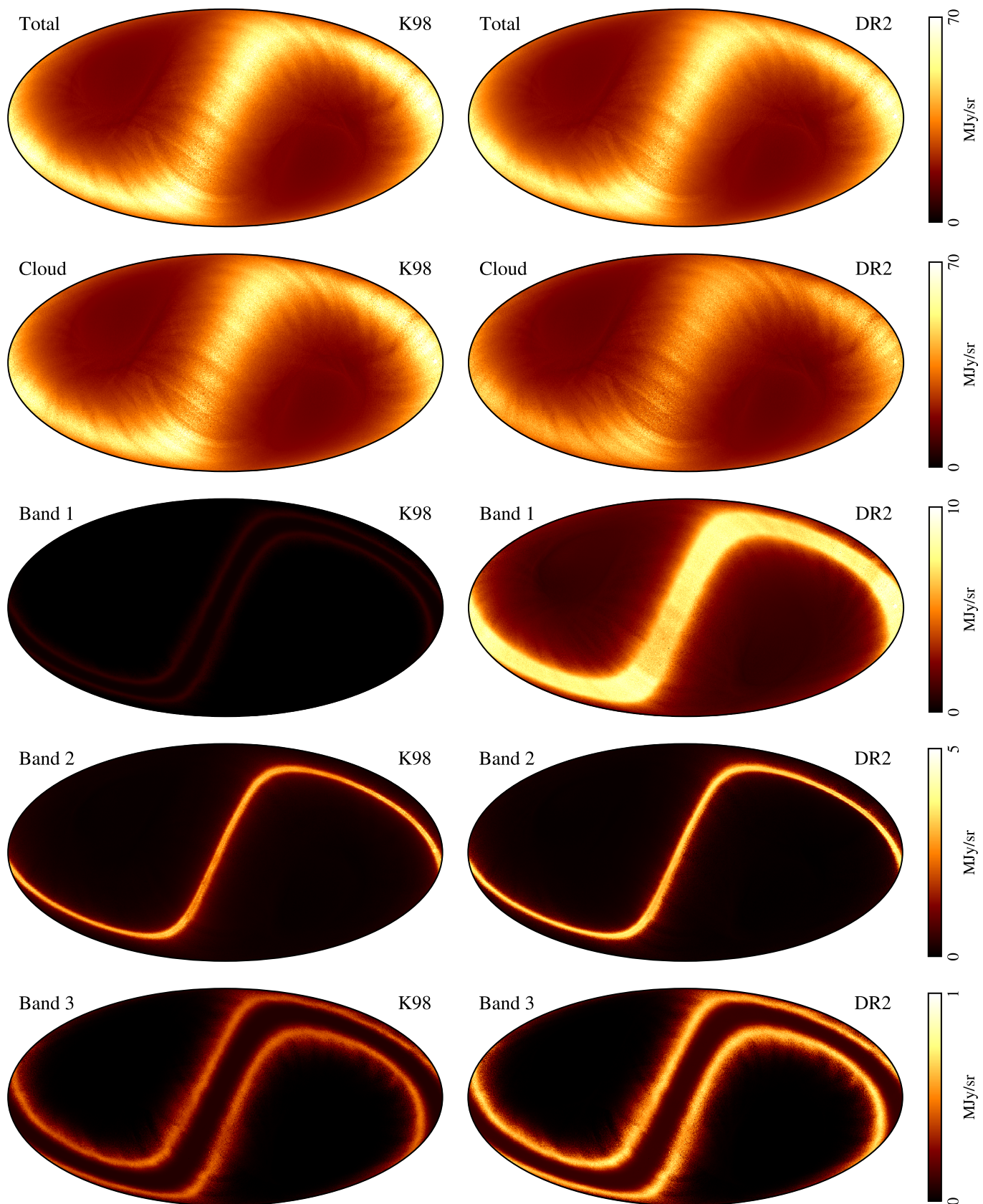


Fig. A.3. Mission-averaged component-wise ZL maps at $25\mu\text{m}$ made with ZodiPy. (*Left column:*) The K98 model. (*Right column:*) Best-fit Cosmoglobe ZL model. Rows list the zodiacal components, from top to bottom, 1) total ZL emission, including the circum-solar ring and Earth-trailing feature; 2) smooth cloud; 3) dust band 1; 4) dust band 2; 5) dust band 3. The maps are in Galactic coordinates.

Appendix B: Interplanetary dust parameter atlas

In this Appendix, we present an atlas of mission-averaged ZL parameter maps. Each map represents the effect of changing one ZL model parameter by $\pm 5\%$ while holding the other fixed. The maps are normalized.

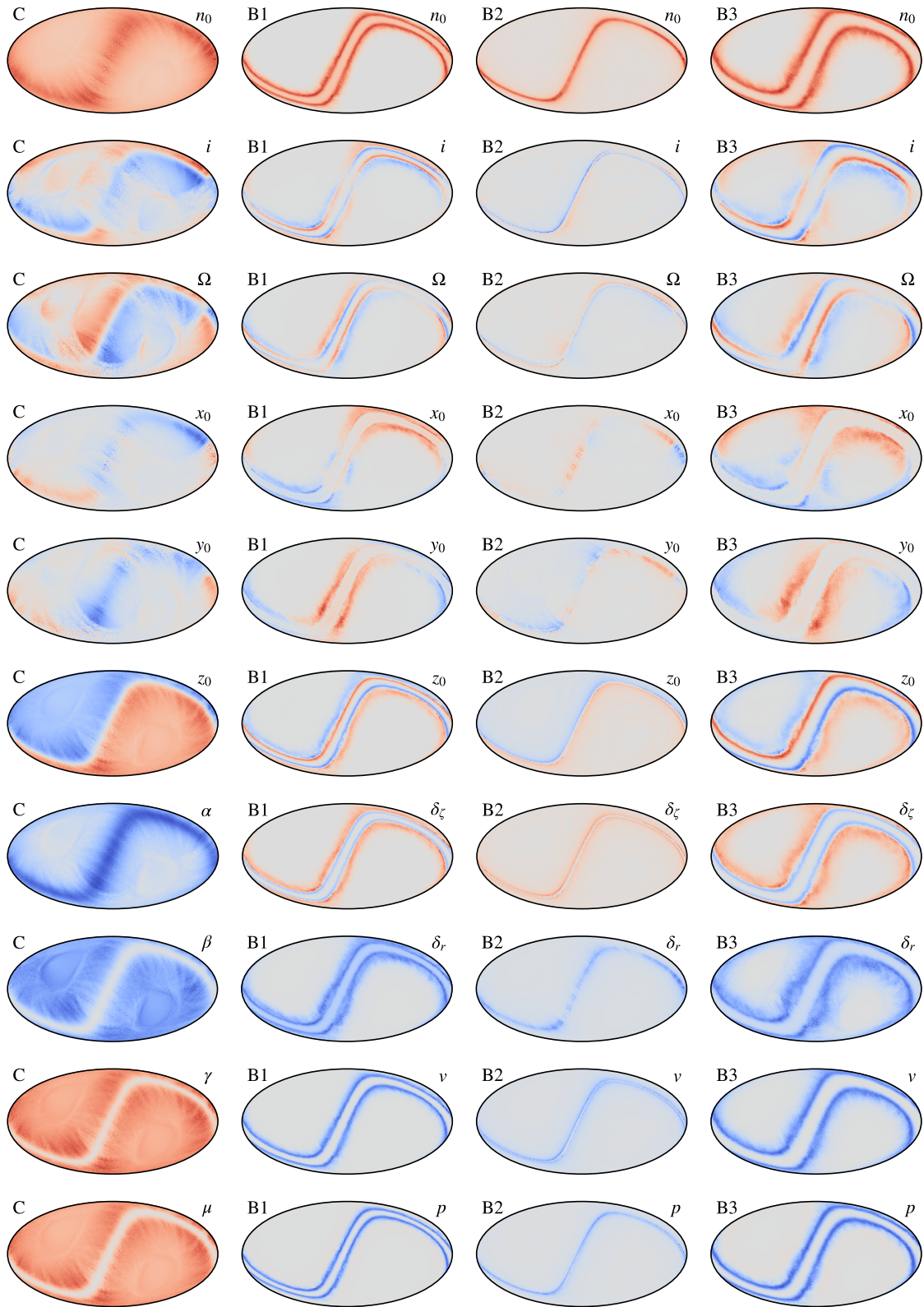


Fig. B.1. ZL parameter atlas showing the difference between increasing and lowering each ZL model parameter by 5% in the form of normalized mission-averaged ZL maps. Columns list, from left to right parameters of 1) the smooth cloud; 2) dust band 1; 3) dust band 2; and 4) dust band 3.

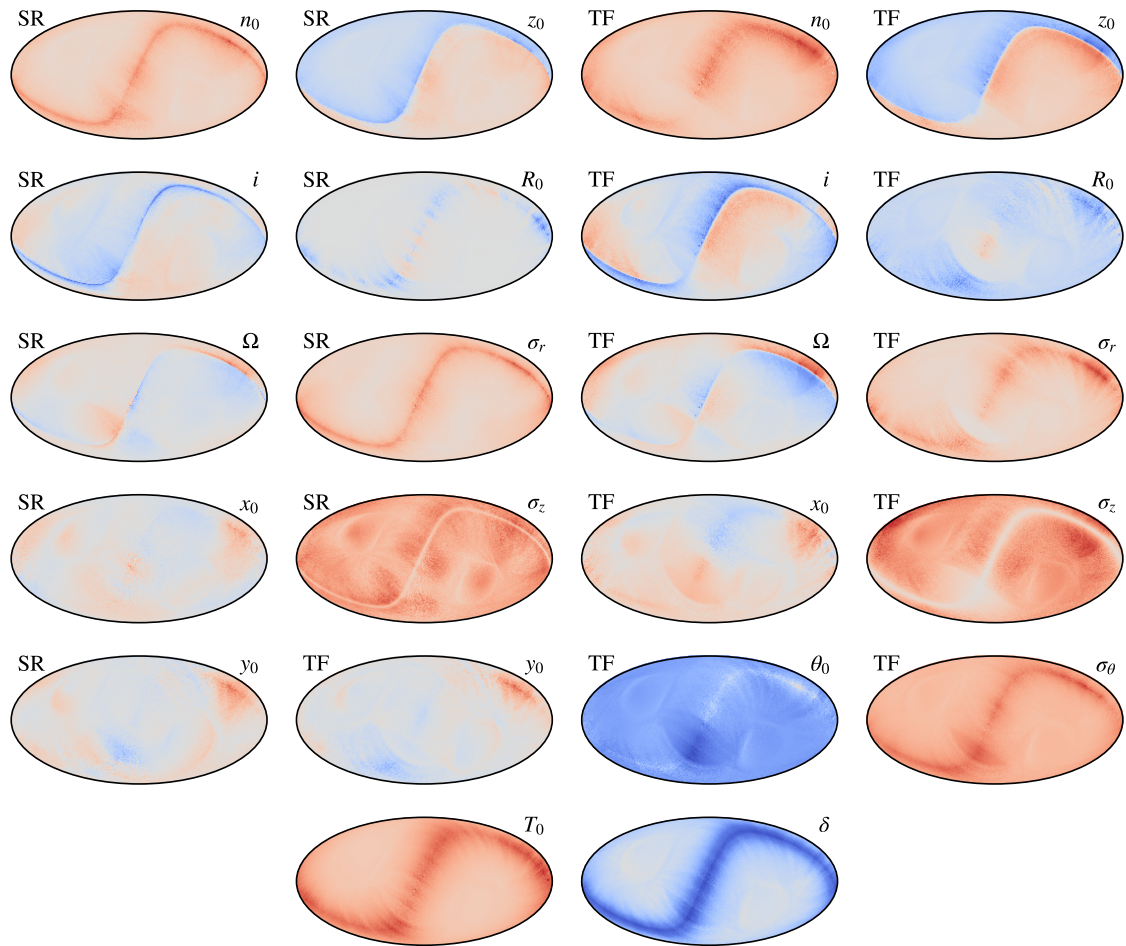


Fig. B.2. ZL parameter atlas showing the difference between increasing and lowering each ZL model parameter by 5% in the form of normalized mission-averaged ZL maps. Columns list the circum-solar ring and Earth-trailing feature components.